

A hard X-ray view of the soft-excess in AGN

Rozenn Boissay¹, Claudio Ricci^{2,3} and Stéphane Paltani¹

¹ Department of Astronomy, University of Geneva, ch. d'Écogia 16, 1290 Versoix, Switzerland

² Pontificia Universidad Católica de Chile, Instituto de Astrofísica, Casilla 306, Santiago 22, Chile

³ EMBIGGEN Anillo, Concepción, Chile

Received; accepted

ABSTRACT

An excess of X-ray emission below 1 keV, called soft-excess, is detected in a large fraction of Seyfert 1-1.5s. The origin of this feature remains debated, as several models have been suggested to explain it, including warm Comptonization and blurred ionized reflection. In order to constrain the origin of this component, we exploit the different behavior of these models above 10 keV. Ionized reflection covers a broad energy range, from the soft X-rays to the hard X-rays, while Comptonization drops very quickly in the soft X-rays. We present here the results of a study done on 102 Seyfert 1s (Sy 1.0, 1.2, 1.5 and NLSy1) from the *Swift* BAT 70-Month Hard X-ray Survey catalog. The joint spectral analysis of *Swift*/BAT and *XMM-Newton* data allows a hard X-ray view of the soft-excess that is present in about 80% of the objects of our sample. We discuss how the soft-excess strength is linked to the reflection at high energy, to the photon index of the primary continuum and to the Eddington ratio. In particular, we find a positive dependence of the soft-excess intensity on the Eddington ratio. We compare our results to simulations of blurred ionized-reflection models and show that they are in contradiction. By stacking both *XMM-Newton* and *Swift*/BAT spectra per soft-excess strength, we see that the shape of reflection at hard X-rays stays constant when the soft-excess varies, showing an absence of link between reflection and soft-excess. We conclude that the ionized-reflection model as the origin of the soft-excess is disadvantaged in favour of the warm Comptonization model in our sample of Seyfert 1s.

Key words. accretion, accretion disks – galaxies: active – galaxies: nuclei – galaxies: Seyferts – X-rays: galaxies

1. Introduction

The typical X-ray spectrum of a Seyfert 1 galaxy is composed of a cut-off power-law continuum, reflection features, low energy absorption and often an excess in the soft X-ray, below 1 keV. The primary continuum power-law is believed to originate from Comptonization of optical/UV photons from the accretion disk by energetic electrons in a hot ($kT \sim 100$ keV), optically-thin ($\tau \sim 0.5$) corona (Blandford et al. 1990; Zdziarski et al. 1995, 1996; Krolik 1999). The reflection component is composed of a Compton hump peaking at ~ 30 keV and fluorescence lines, the most important of which is the Fe $K\alpha$ line around 6-7 keV. This reflection can be due to reprocessing of the primary X-ray continuum on distant neutral material such as the molecular torus present in the unification model (Antonucci 1993; Jaffe et al. 2004; Meisenheimer et al. 2007; Raban et al. 2009), on the broad- and narrow-line regions (Bianchi et al. 2008; Ponti et al. 2013) or in the accretion disk (George & Fabian 1991; Matt et al. 1991).

While Seyfert 2 galaxies are generally highly absorbed, for example by the dusty torus requested by the unification model (Antonucci 1993), Seyfert 1s are usually non or lightly absorbed ($N_H \leq 10^{22}$ atoms cm^{-2}). When the absorbing material is photoionized, it is referred to as warm absorber (George et al. 1998). Absence of absorption allows us to see a soft X-ray emission in excess of the extrapolation of the hard X-ray continuum in many Seyfert 1s below 1 keV. Discovered by Singh et al. (1985) and Arnaud et al. (1985) using *HEAO-I* and *EXOSAT* observations, this feature has since then been called *soft-excess* (SE) and is detected in more than 50% of Seyfert 1s (Halpern 1984; Turner & Pounds 1989). This fraction can reach 75% to 90% according

to Piconcelli et al. (2005), Bianchi et al. (2009) and Scott et al. (2012). The soft-excess was first believed to originate in the inner part of the accretion flow (Arnaud et al. 1985; Pounds et al. 1986) and it has been modeled for a long time using a blackbody with temperatures of $\sim 0.1 - 0.2$ keV. This model has been ruled out since a standard accretion disk around a supermassive black hole can not lead to such high temperatures (Shakura & Sunyaev 1973). Moreover, the temperature of the blackbody used to model the soft-excess has been found to be independent of the black-hole mass, in opposition with what is expected from a standard accretion disk (Gierliński & Done 2004).

A possible explanation for the soft-excess is the “warm” Comptonization scenario: UV seed photons from the disk are up-scattered by a Comptonizing corona cooler and optically thicker than the hot corona responsible for the primary X-ray emission. This model has been successfully applied to NGC 5548 (Magdziarz et al. 1998), RE J1034+396 (Middleton et al. 2009), RX J0136.9–3510 (Jin et al. 2009), Ark 120 (Matt et al. 2014) and 1H 0419–577 (Di Gesu et al. 2014). This Comptonization model is supported by the existence of similarities between the spectral shape (Walter & Fink 1993) and the variability of the optical/UV and soft X-ray emission (Edelson et al. 1996). In a more recent work, Mehdipour et al. (2011) found, in the framework of a multi-wavelength campaign on Mrk 509, a strong correlation between fluxes in the optical/UV and soft X-ray bands, as it would be expected if the soft-excess is due to warm Comptonization of the seed photons from the disk. Petrucci et al. (2013) found, using ten simultaneous *XMM-Newton* and *INTEGRAL* observations of Mrk 509, that a hot ($kT \sim 100$ keV), optically-thin ($\tau \sim 0.5$) corona is producing the primary contin-

uum and that the soft-excess can be well modeled by a warm (kT \sim 1 keV), optically-thick ($\tau \sim$ 10-20) plasma. A warm Comptonization model is also confirmed in Mrk 509 by considering the excess variability in the soft-excess flux on long time scales and variability properties in general (Boissay et al. 2014). Using five observations of Mrk 509 with *Suzaku*, Noda et al. (2011) showed that the fast variability seen in hard X-rays is not present in the soft X-ray excess. This differential variability rules out a small reflector origin for the soft-excess in Mrk 509, similarly to what has been shown by Boissay et al. (2014), because the soft X-rays should closely follow the hard X-ray variability in the relativistic ionized reflection models.

As the Comptonization hypothesis has difficulties to explain the consistency of the soft-excess feature over a large range of black-hole masses M_{BH} , another possible explanation for the soft-excess, blurred ionized reflection, has been invoked. In this scenario, the emission lines produced in the inner part of the ionized disk are blurred by the proximity of the supermassive black hole (SMBH). Crummy et al. (2006) successfully applied such an ionized-reflection model (`reflionx`; Ross & Fabian 2005) on a sample of PG quasars to explain the soft-excess. Zoghbi et al. (2008) used a similar approach for Mrk 478 and EXO 1346.2+2645. This model has been used to explain the spectral shape, as well as the variability, in MCG-6-30-15 (Vaughan & Fabian 2004) and NGC 4051 (Ponti et al. 2006). Walton et al. (2013) used a sample of 25 bare AGN observed with *Suzaku* to test the robustness of the reflection interpretation, by reproducing the broad-band spectra using the `reflionx` model (as done by Crummy et al. 2006), and to constrain the black hole spin in many objects of the sample. More advanced blurred ionized-reflection models have been created in recent years, such as `relxill`, developed by García et al. (2014) and Dauser et al. (2014), that merges the angle-dependent reflection model `xillver` with relativistic blurring model `reline`. This `relxill` model has already been used to explain the soft-excess in Mrk 335 (Parker et al. 2014) and in SWIFT J2127.4+5654 (Marinucci et al. 2014). Vasudevan et al. (2014) showed, using *Swift/BAT* observations and *XMM-Newton/NuSTAR* simulations, that a correlation between the reflection and the soft-excess strength is expected if this feature is due to blurred ionized reflection. Parameters obtained when fitting spectra with ionized-reflection models are often extreme. A maximally rotating supermassive black hole and a very steep emissivity are required in most cases (Fabian et al. 2004; Crummy et al. 2006), as well as fine-tuning of the ionization of the disk (Done & Nayakshin 2007). These parameters, similar to those obtained when modelling the broad component of the Fe K α line (Fabian et al. 2005), show that in this scenario most of the reprocessed radiation is produced very close to the event horizon. Time delays between iron lines and direct X-ray continuum have been detected in several objects (e.g. 1H 0707-495, Fabian et al. 2009; NGC 4151, Zoghbi et al. 2012; MCG-5-23-16 and NGC 7314, Zoghbi et al. 2013; Ark 564 and Mrk 335, Kara et al. 2013). Soft X-ray reverberation lags have been detected in a considerable sample of objects (Cackett et al. 2013; de Marco et al. 2011; De Marco et al. 2013) and are interpreted as being a signature of reverberation from the disk, which would support the reflection origin for the soft-excess. However, if soft lags are detected on short time scales, the soft X-ray emission can lead the hard band on long time scales, as in PG 1244+026 (Gardner & Done 2014). In this case, the soft-excess is interpreted as a combination of intrinsic fluctuations propagating down through the accretion flow giving the soft lag and reflection of the hard X-ray emission giving the soft lag.

Using a sample of six bare Seyfert galaxies, Patrick et al. (2011) modeled the *Suzaku* broad-band spectra with both ionized reflection and additional Compton scattering components. Combining the two models to reproduce the soft-excess provided better fitting results with lower values of spin and emissivity index. Other works presenting direct tests of the ionized reflection versus warm Comptonization include for example analyses from Lohfink et al. (2013) and Noda et al. (2013). Lohfink et al. (2013) used archival *XMM-Newton* and *Suzaku* observations of Mrk 841 to test different models for the origin of the soft-excess in a multi-epoch fitting procedure. Noda et al. (2013) fitted *Suzaku* spectra of five AGN with different models to reproduce the soft-excess, concluding that the thermal Comptonization model reproduces better the data.

The soft-excess could also be the signature of strong, relativistically smeared, partially ionized absorption in a wind from the inner disk, as proposed for PG 1211+143 by Gierliński & Done (2004). In the case of a totally covering absorber, extreme parameters are needed to reproduce the observed soft-excess, as in the case of blurred ionized-reflection models. For example, a very high smearing velocity ($v \sim 0.3c$) is required, but such a velocity is difficult to reach considering radiatively driven accretion disk winds (Schurch & Done 2007; Schurch et al. 2009). We shall not further discuss this model in this paper.

This paper aims to test blurred ionized-reflection models as the origin of the soft-excess, in particular in the lamp-post configuration, via a spectral model-independent analysis. Different scenarios of the origin of the soft-excess imply different behaviors in the soft and hard X-ray bands, as ionized reflection covers a broad energy range, while Comptonization drops very quickly in the soft X-rays. As we want to get good constraints on the hard X-ray reflection measurements, we consider sources detected by the *Swift/BAT* instrument and combine these observations with data from the *XMM-Newton* satellite, in order to get information about the soft-excess. We carry out broad-band (0.5-100 keV) spectral analysis of the sources and explore the relations between the parameters resulting from the fitting procedure. We compare the reflection and soft-excess parameters with those obtained from simulations in a lamp-post configuration. We also study the differences between soft and hard X-ray emission by stacking the XMM and BAT spectra according to their soft-excess strengths.

2. Sample and data analysis

We use a sample of sources from the *Swift* (Gehrels et al. 2004) *BAT* 70-Month Hard X-ray Survey catalog (Baumgartner et al. 2013), which contains 1210 sources including 292 Seyfert 1s. By cross-correlating the *Swift/BAT* catalog with the Veron catalog (Véron-Cetty & Véron 2010), we select only Narrow-line Seyfert 1s (NLSy1s) and Seyfert 1s - 1.5s (Sy1s - 1.5s). Our sample is in this way composed of 102 sources, divided in 37 Sy1.0s, 18 Sy1.2s, 35 Sy1.5s and 12 NLSy1s. We select sources that have been observed with the *XMM-Newton* satellite (Jansen et al. 2001) as pointed observations with a minimum exposure time of 5 ks (see Tab .2). We select sources with a flux higher than 10^{-11} ergs/s/cm² in the 14-195 keV band. *BAT* spectra (Barthelmy et al. 2005) have been obtained from the *Swift/BAT* website ¹.

In order to study the soft X-ray emission of these objects, we use XMM-Newton observations. In the case of multiple observations for the same source, we consider the observation

¹ <http://Swift.gsfc.nasa.gov/results/bs70mon/>

with the longest exposure time (see Tab .2). Data reduction is performed on the original data files using the *XMM-Newton* Standard Analysis Software (SAS v12.0.1 - Gabriel et al. 2004) considering both *PN* (Strüder et al. 2001) and *MOS* (Turner et al. 2001) spectra of each source. Events are filtered using #XMMEA_EP and #XMMEA_EM, for *PN* and *MOS* cameras respectively. Single and double events are selected for extracting *PN* spectra and single, double, triple and quadruple events are considered for *MOS*. The data are screened for any increased flux of background particles. Spectra are extracted from a circular region of 30 arcsec centred on the source. The background is extracted from a nearby source-free region of 40 arcsec in the same CCD as the source. The *XMM-Newton* data show evidence of significant pile-up in some objects (see Tab .2), for which the extraction region used is an annulus of inner radius 15 arcsec instead of a simple circle. Response matrices are generated for each source spectrum using the SAS *arfgen* and *rmfgen* tasks.

3. Spectral analysis

In this section, we explain the broad-band spectral analysis procedure of all the sources of our sample between 0.5 and 100 keV. More precisely, we fit the 3-100 keV data with a phenomenological model and then quantify the soft-excess below 2 keV with respect to this model. We present different fitting models taking into account reprocessing mainly due to distant and/or local reflectors.

3.1. Spectral fitting procedure

3.1.1. Reprocessing mainly due to a distant reflector

The spectral analysis of our sample is performed using the general X-ray spectral-fitting program XSPEC (version 12.8.1, Arnaud 1996). In order to determine specific parameters for each object of our sample, we analyse *PN* and *MOS* spectra from the *XMM-Newton* satellite and *BAT* spectra from *Swift*.

We first choose to fit jointly *PN/MOS* and *BAT* spectra in an energy band in which there is little contamination from the soft-excess or absorption (from 3 to 100 keV) with a cut-off power-law and a neutral reflection component using the *pexmon* model (Nandra et al. 2007) from XSPEC. The *pexmon* model is similar to the *pexrav* model (Magdziarz & Zdziarski 1995), but includes Fe $K\alpha$, Fe $K\beta$ and Ni $K\alpha$ lines and the Fe $K\alpha$ Compton shoulder (George & Fabian 1991). We use the *pexmon* model to take into account the reflection component, the cut-off power-law component being modeled by *cutoffpl*. We also take into account Galactic absorption (abs_{Gal}), fixing the value of N_{H}^{G} to the one found in the literature (Dickey & Lockman 1990) (see Tab .2).

The *pexmon* model includes the narrow iron lines produced by reflection from distant neutral material, such as the broad-line region (e.g. Bianchi et al. 2008), the molecular torus (e.g. Shu et al. 2011; Ricci et al. 2014) or the region between the torus and the broad-line region (Gandhi et al. 2015). However, assuming that the primary X-ray continuum is also reprocessed in the innermost part of the accretion disk, these iron lines should be broadened by Doppler motion and relativistic effects (e.g. Fabian et al. 1989). To take into account these effects, we allow broadening of the iron line from *pexmon*, by convolving the *pexmon* model with a Gaussian smoothing model *gsmooth* (σ can vary between 0.0 and 0.5 keV).

XMM-Newton and *Swift/BAT* observations are not simultaneous, as *BAT* spectra are integrated over 70 months, so vari-

ability in flux can occur between *XMM-Newton* and *Swift/BAT* spectra. To correct the flux variability during the fitting procedure, we multiply the cut-off power-law of our model by a cross-calibration factor f . The *pexmon* component parameters are fixed to the same value for *XMM-Newton* and *BAT*. Doing so, we consider that the reflection component, assumed to be mainly due to a distant reflector, does not vary during the *BAT* time scale and that only the primary continuum does. The cross-calibration factor f is fixed to 1 for *BAT* spectra and let free between 0.7 and 1.3 for *XMM-Newton* spectra (f is found to be consistent with being equal for *PN* and *MOS* spectra). Using this f factor, we constrain sufficiently the fit while taking into account the flux variability of the primary continuum between *XMM-Newton* and *BAT*.

The resulting model for the fit between 3 and 100 keV is:

$$\text{abs}_{\text{Gal}} (f \times \text{cutoffpl} + \text{gsmooth} * \text{pexmon})$$

When fitting the *XMM-Newton* and *Swift/BAT* spectra between 3 and 100 keV, we keep the inclination angle of the disk to its default value of 60° . Abundances in *pexmon* are free to vary between 0.3 and 3 (relative to Solar), in order to properly model the iron line as well as the Compton hump. The high-energy cut-off can vary from 100 to 500 keV. The reflection factor R , which is the strength of the reflection component relative to that expected from a slab subtending 2π solid angle, can have values between 0 and 100. We find the best fit parameter values using the χ^2 statistics of XSPEC.

In order to study the soft X-ray emission of the objects, we fix the parameters of the model described previously to the values found during the fit between 3 and 100 keV and add *XMM-Newton* data in the 0.5 to 3 keV energy band. We remove the *gsmooth* component from our model to avoid spurious features at low energy (arising from the convolution at the edge of the spectrum). Suppressing this component will just slightly degrade the χ^2 value and give an advantage in computation time. As we want this analysis to be model independent, we do not favour any hypothesis here for the origin of the soft-excess. In order to measure the strength of the soft-excess, we use a Bremsstrahlung model which provides a good phenomenological representation of its smooth spectral shape. We then find the best-fit parameter values using the χ^2 statistics, fitting the spectra between 0.5 and 100 keV. In the majority of the objects of our sample, the soft-excess is better fitted by two Bremsstrahlung models than by a single one, with plasma temperatures between 0 and 1 keV.

We also evaluate the presence of absorption from a cold or ionized medium ($\text{abs}_{\text{cold/warm}}$). The presence of a single or double warm absorber (WA), modeled by *XSTAR* and/or of a cold absorber, modeled by *zfabs*, is verified by a F-test between the model taking into account the soft-excess only and the one including the absorber.

The resulting broad-band fitting model is:

$$\text{abs}_{\text{Gal}} \times \text{abs}_{\text{cold/warm}} (\text{bremss} + \text{bremss} + f \times \text{cutoffpl} + \text{pexmon})$$

3.1.2. Reprocessing mainly due to a local reflector

In Sect. 3.1.1, we consider that the reflection component is mainly due to a distant reflector, which is expressed by the cross-calibration being applied to the power-law and not to the *pexmon* component in the fitting procedure. We also want to study the case where the reflection is mainly due to a local reflector. The model used for this hypothesis to fit the 3 to 100 keV band is:

$$\text{abs}_{\text{Gal}} \times f(\text{cutoffpl} + \text{gsmooth} * \text{pexmon})$$

Applying this f cross-calibration factor on the `pexmon` component allows this time to consider that the reflection responds with very little lag to the continuum. We fit this new model on our objects with the same ranges of parameters as described in Sect. 3.1.1. The fitting procedure between 0.5 and 100 keV is the same as the one described in Sect. 3.1.1, with the model:

$$\text{abs}_{\text{Gal}} \times \text{abs}_{\text{cold/warm}}(\text{bremss} + \text{bremss} + f(\text{cutoffpl} + \text{pexmon}))$$

3.1.3. Comparison between local and distant reflection models

For each object of our sample we perform a statistical F-test between models of local and distant reflection. We can see in Fig. 1 that, considering the theoretical F values range from the Fisher table for which we can accept the null hypothesis at a 95% significance level (see red area in Fig. 1), only 8% of our objects are better fitted by the local reflection model and 3% by the distant reflection model. The average value of F being smaller than 1 ($F_{\text{mean}}=0.98$) shows a little preference for the local-reflection model to fit our data, but as F_{mean} is inside the acceptance zone, this preference is not significant. We therefore cannot distinguish between the local-reflection and the distant-reflection models here.

The X-ray spectra of our Seyfert galaxies should present iron emission lines with two components: the narrow line coming from reflection on the dusty torus or on broad-line region, and the broad line thought to be produced in the inner accretion disk. The total reflection factor includes the reflection strengths of both components. In the hypothesis where the soft-excess is due to ionized reflection, the broad line is expected to be more important than the narrow one, that is why we use a `gsmooth` model to allow the broadening of the iron line from the `pexmon` model. Furthermore, we have just seen that changing the input of the cross-calibration factor to account for local and distant reflections does not allow to distinguish the models. However, in order

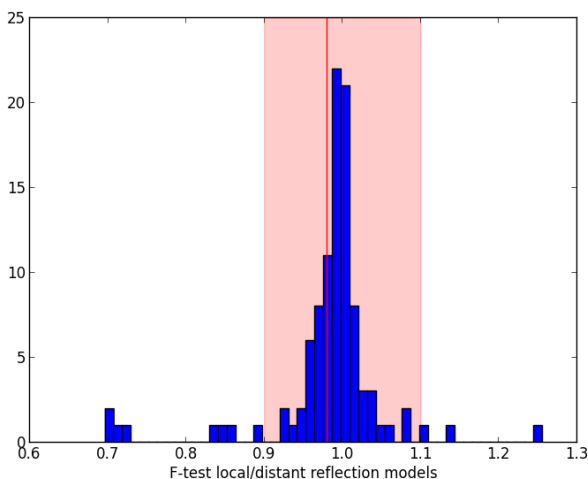


Fig. 1. Distribution of the F-test results between the local reflection model and the distant reflection model used to fit each object. The red area is the acceptance zone of the null-hypothesis. The average F value, represented by the red line, is inside the acceptance zone.

to check that we do not miss any information from the narrow iron lines, we test a fitting procedure with two `pexmon` models on 10% of the objects of our sample. One simple `pexmon` model is used to reproduce the narrow iron line, and the second one, convolved with a `gsmooth` model, represents the broad component. The sum of the reflection fractions from the two `pexmon` models is equal to the reflection fraction measured with our one-`pexmon` fitting procedure. This test has been done on ten objects for which we have good signal-to-noise data. As the results are consistent between the two approaches and as the reflection factor is better constrained in our initial fitting procedure, we choose to keep this one-reflection fitting process to model our data.

3.2. Soft-excess and absorption properties

The results obtained by our spectral analysis, under the hypothesis of a reflection mainly due to distant material, are presented in Tab .3. We find that 79 objects (i.e. 80% of our sample) present a soft-excess (SE). Among these 79 objects showing a soft-excess, 42 do not show the presence of absorption and 37 are lowly absorbed by cold or warm material.

The 24 other objects show the presence of a stronger absorption by a cold or warm absorber with a column density value $N_{\text{H}} \geq 10^{22}$ atoms cm^{-2} . These absorbers prevent a good measurement of an eventual soft-excess. Twelve of these strongly absorbed objects present a complex absorption and are labeled in Tab .3:

- (a) ESO 323–77: Miniutti et al. (2014) used multi-epoch spectra from 2006 to 2013 to show that the absorption is due to a clumpy torus, broad-line regions and two warm absorbers.
- (b) EXO 055620–3820.2: Turner et al. (1996) found by using *ASCA* observations that the continuum of the source is attenuated by an ionized absorber either fully or partially covering the X-ray source.
- (c) IC 4329A: Steenbrugge et al. (2005) showed, using *XMM-Newton* observations, that the absorber is composed of seven different absorbing systems.
- (d) MCG–6–30–15: Miyakawa et al. (2012) fitted *Suzaku* data considering absorbers with only a variable covering factor.
- (e) Mrk 1040: Reynolds et al. (1995) found that the soft spectral complexity visible in *ASCA* observations could be either explained by a soft-excess and intrinsic absorption, or by a complex absorber.
- (f) Mrk 6: Mingo et al. (2011) showed that the variable absorption visible in *XMM-Newton* and *Chandra* observations is probably caused by a clump of gas close to the central AGN in our line of sight.
- (g) NGC 3227: Beuchert et al. (2014) used *Suzaku* and *Swift* observations of a 2008 eclipse event to characterize the variable-density absorption, probably due to a filamentary, partially covering and moderately ionized cloud.
- (h) NGC 3516: Huerta et al. (2014) showed that this object is absorbed by four warm absorbers, according to nine *XMM-Newton* and *Chandra* observations.
- (i) NGC 3783: Brenneman et al. (2011) used *Suzaku* observations to show the presence of a multicomponent warm absorber.
- (j) NGC 4051: Pounds & King (2013) found, using a *XMM-Newton* observation, a fast, highly ionized wind, launched from the vicinity of the supermassive black hole, that shocked against the interstellar medium (ISM). They specu-

late that the warm absorbers often observed in AGN spectra result from an accumulation of such shocked winds.

- (k) NGC 4151: Wang et al. (2011) found, in a Chandra observation, emission features in soft X-rays that are consistent with blended brighter O VII, O VIII and Ne IX lines. They also found low and high ionization spectral components that are consistent with warm absorbers.
- (l) UGC 3142: Ricci et al. (2010) used *XMM-Newton*, *Swift* and INTEGRAL data for the spectral analysis. This object is absorbed by two layers of neutral material.

We decide not to include these 23 absorbed objects in our analysis in order to have a clean measurement of the soft-excess intensity.

3.3. Soft-excess strength

We keep for the following analysis only the 79 objects showing presence of soft-excess and absorbed by a material with a N_{H} smaller than 10^{22} atoms cm^{-2} . For each of these objects, we define the strength of the soft-excess q as the ratio between the flux of the soft-excess (i.e. the flux of the Bremsstrahlung models between 0.5 and 2 keV) and the extrapolated flux of the continuum between 0.5 and 2 keV. This definition differs from the one used in Vasudevan et al. (2014), as discussed in Sect. 4.2.

4. Relation between reflection and soft-excess strength

In this section, we compare the reflection and soft-excess strength from data with those obtained from simulations of blurred ionized reflection. These simulations, similar to the ones of Vasudevan et al. (2014), are performed using the lamp-post configuration of the *relxill* model of García et al. (2014) and Dauser et al. (2014), changing the height of the source which controls the emissivity index and the reflection fraction, and changing the mass accretion rate which controls the inner disk ionization. The resulting simulated spectra are then fitted with the same phenomenological model than real data, in order to compare the distributions of soft-excess strength versus reflection strength from the real and simulated data.

4.1. R vs q in the sample

To study the evolution of the soft-excess with reflection, we plot in top panel of Fig. 2 the reflection factor measured when fitting *XMM-Newton* (*EPIC PN* and *MOS*) and *Swift/BAT* spectra as a function of the soft-excess strength q . In the case of distant reflection (see Sect. 3.1.1), we find an anti-correlation characterized by a Spearman coefficient of $r=-0.33$ and a null-hypothesis probability of about 0.3%. We perform a bootstrap on the data, finding a 99.9% Confidence Interval (CI) for the Spearman correlation coefficient of $-0.62 \leq r \leq 0.01$ and a probability to have a negative correlation of 99.8%.

Note that our sample includes NLSy1s, objects that often present a strong soft-excess and a steep spectrum (e.g. Vaughan et al. 1999; Haba et al. 2008; Done et al. 2013). If we do not include the 10 NLSy1s in our analysis, we still find a correlation with a Spearman coefficient of $r = -0.31$, a null-hypothesis probability of about 0.7% and a probability of 99% to have a negative correlation between R and q .

In order to look at the effect of the warm absorber in the objects of our sample, we only consider the 42 objects showing a

soft-excess without absorber. Spearman statistics give a correlation coefficient of $r=-0.37$ with a null-hypothesis probability of 2% and the probability of having a negative correlation of 98%. The anti-correlation between R and q found with the entire sample of objects showing a soft-excess with or without absorber still exists when considering only objects without absorber. In this case, the anti-correlation is less significant, as it is based on about half of the sample.

In order to take into account errors in both x and y axes, as well as intrinsic scatter, we perform a linear regression with a Bayesian approach using an IDL procedure called *linmix_err* (Kelly 2007). The linear regression process results in the relation:

$$R = -0.72_{-0.21}^{+0.28} \times q + 1.01_{-0.11}^{+0.18} \quad (1)$$

The intrinsic scatter of R is 0.37. The Markov Chains Monte Carlo (MCMC) created by the IDL procedure allow us to plot the 99.9% CI for this linear regression (blue contours in top panel of Fig. 2).

In the case of local reflection (see Sect. 3.1.2), Spearman statistics give a correlation coefficient of $r=-0.48$ between R and q and a null-hypothesis probability of 0.06%. The linear regression performed with *linmix_err* results in the relation:

$$R = -0.54_{-0.12}^{+0.09} \times q + 0.94_{-0.01}^{+0.20} \quad (2)$$

The intrinsic scatter of R is 0.24.

If we only consider NLSy1 galaxies, Spearman statistics give a correlation coefficient of $r=-0.36$, a null-hypothesis probability of 31% and a probability of 87% to have a negative correlation. The significance of this result is still quite strong considering the fact that our sample contains only 10 NLSy1s for which we can measure the soft-excess.

4.2. R vs q in simulations of ionized reflection

Vasudevan et al. (2014) performed ~ 2400 *XMM-Newton* and *NuSTAR* simulations of blurred ionized reflection, using *reflionx* and *kdblur*, taking into account neutral reflection with *pexrav*. They used a large range of values for the iron abundance, the photon index, the ionization and the ratio between the normalizations of *pexrav* and *reflionx*. They fixed the emissivity index and the inclination to intermediate values and fixed the high energy cut-off to 10^6 keV. The strength of the hard excess R was then measured by a neutral reflection model *pexrav* (the iron line being modeled by a Gaussian component) and the soft-excess was modeled by a blackbody. They fixed the normalizations of each component of this model, in order to constrain the blackbody temperature and the Gaussian line energy and width. They defined the soft-excess strength as being the ratio between the luminosity from the blackbody between 0.4 and 3 keV and the power-law luminosity between 1.5 and 6 keV. Their simulations predict the existence of a correlation between R and the soft-excess strength.

We want to determine the expected relation between the reflection factor and the soft-excess strength in the case of ionized reflection, similarly to what was done by Vasudevan et al. (2014). But as we want to use a more recent ionized-reflection model and as our spectral fitting procedure differs from the one of Vasudevan et al. (2014), we perform simulations using the *relxillp.ion* model. The *relxillp.ion* model (Dauser et al. 2014) is similar to the *relxill* model, but adapted for the lamp-post geometry. By simulating this lamp-post configuration, we assume an explicit link between the smearing and the amount of reflection. For example, for objects such as 1H 0707–495,

that have a high emissivity index and are thus strongly smeared, the compact source is thought to be confined to a small region around the rotation axis and close to the black hole (Fabian et al. 2012). The very small height h required predicts a very large reflection fraction R (see the relation between R and h plotted in Figure 2 of Dauser et al. 2014). The ionization of the accretion disk depends on the mass accretion rate \dot{m} and on the density profile of the disk. The density structure assumed in a hydrostatic α -disk (Shakura & Sunyaev 1973) is not always appropriate. In particular, it has been shown that the accretion disk cannot be in hydrostatic equilibrium if the soft-excess is made via reflection (Done & Nayakshin 2007). In the `relxillp_ion` model, the ionization gradient is calculated self-consistently from the irradiation of the disk (using a certain mass accretion rate \dot{m}),

and the density distribution does no longer follow the hydrostatic equilibrium assumption, but its power-law index is rather fitted directly to the data.

We simulate *Swift/BAT* and *XMM-Newton/PN* spectra with a signal-to-noise ratio comparable to our data (time exposure of 10 ks for *XMM-Newton/PN* and 1 Ms for *Swift/BAT*). We perform ~ 3500 simulations with different values of `relxillp_ion` parameters for the reflection factor R_{rel} (from 0 to 100, values which are reachable in a lamp-post configuration for a source very close to the black hole, see Fig. 5 in Miniutti & Fabian 2004), the photon index Γ_{rel} (from 1.4 to 2.5), the ionization parameter at the inner edge of the disk [$\log(\xi)$ between 0.0 and 4.7, as allowed by the model], the abundances A_{Fe} (from 0.3 to 3.0 in solar unit), the height h of the source (from 1 to $6 r_g$), the inner radius R_{in} (from 1 to $50 r_g$), the density index (from 0 to 4), the mass accretion rate \dot{m} (from 0.01 to 5) and the high-energy cut-off $E_{c,rel}$ (from 100 to 300 keV). In order to account for the narrow component of the iron line in our simulated spectra, we add to our `relxillp_ion` model a `pexmon` component, to reproduce the neutral reflection on the dusty torus and broad-line regions, with a reflection factor R_{narrow} varying between 0 and 1. Considering only Seyfert 1s and according to the unification model, we perform simulations for different inclination values θ between 0° and 60° , giving to each simulation the weight $\sin(\theta)$ to take into account the probability of having such an inclination.

We fit our simulated `relxillp_ion` spectra by using the fitting procedure explained in Sect. 3.1, in order to measure the photon index and the reflection from the `pexmon` model, as well as the value of the soft-excess strength q and to be able to compare them to the parameters obtained when fitting the real data. We perform a linear regression (red solid line in top panel of Fig. 2) and plot density contours of the simulated data (red contours in top panel of Fig. 2; solid line: 68%, dashed line: 90%). Similarly to Vasudevan et al. (2014), we expect to find a positive correlation between the reflection factor R and the soft-excess strength q , if ionized reflection model is the explanation of the soft-excess, even if the simulations and the soft-excess strength definition are slightly different. We find such a positive correlation with our simulations, assuming all `relxillp_ion` parameters are uncorrelated. Spearman statistics give a correlation coefficient between R and q expected for ionized-reflection model of $r=0.55$ and a negligible null-hypothesis probability. The expected relation is:

$$R = 6.17^{+0.19}_{-0.20} \times q + 2.80^{+0.11}_{-0.11} \quad (3)$$

Bottom panel of Fig. 2 shows the reflection factor R measured by `pexmon` as a function of the soft-excess strength q , for real and simulated data. Blue points represent the real data, i.e. results of the fitting of the objects of our sample and red triangles are the parameters obtained by simulating `relxillp_ion` models (red contour in top panel of Fig. 2 has been derived from these red triangles). As we can see in bottom panel of Fig. 2, 75% of the blue data points are contained in the blue box ($R < 2.0$ and $q < 0.75$). `Relxillp_ion` simulations result in similar parameters, but also in higher reflection factors and higher soft-excess strengths. 25% of our simulated objects are in the blue box and 75% of them are outside the blue box. We do not observe any high- R objects, contrarily to what is expected with blurred ionized-reflection models (with the `relxillp_ion` model in our simulations, and with the `reflionx` model in simulations from Vasudevan et al. 2014).

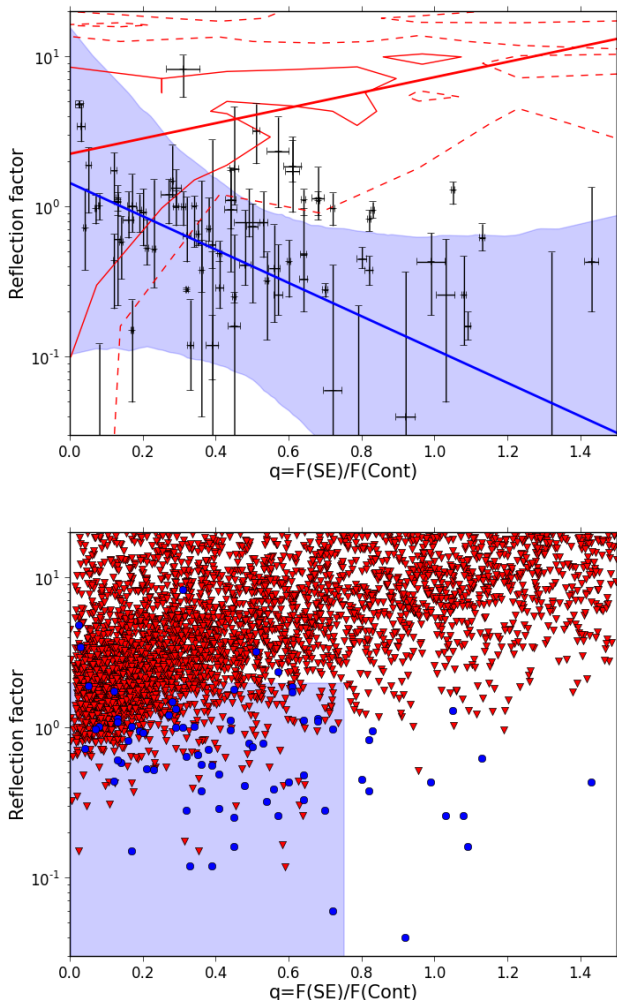


Fig. 2. Reflection factor R as a function of the strength of the soft-excess q (in the case of distant reflection). Top panel: Linear regression performed using the `linmix_err` procedure is represented by the blue line and 99.9% CI is given by the blue contour. The red line represents the positive correlation expected if the soft-excess is due to ionized reflection (result of `relxillp_ion` simulations, see Sect. 4.2). Density contours of the simulations are plotted in red (solid line: 68%; dashed line: 90%). Bottom panel: Blue points represent our 79 objects showing a soft-excess. They are mostly contained (75%) in the blue box ($R < 2.0$ and $q < 0.75$). Red triangles are `relxillp_ion` simulation results.

5. Evolution of the photon index of the primary continuum

In this section, we explore the relations between the photon index of the primary continuum, and the reflection and soft-excess strength. We compare the parameters derived from data analysis with those obtained from simulations of lamp-post configuration.

5.1. Soft-excess and photon index

We plot in Fig. 3 the photon index of the primary continuum as a function of the soft-excess strength q (in the case of distant reflection). This plot reveals a hint of a weak correlation between Γ and q . Indeed, Spearman rank analysis gives a correlation coefficient of $r=0.19$ and a null-hypothesis probability of about 10%. A bootstrap on the data points gives a probability of 91% to have a positive correlation. We use the Bayesian `linmix_err` procedure to perform a linear regression. We obtain

$$\Gamma = 0.14^{+0.05}_{-0.06} \times q + 1.65^{+0.04}_{-0.02} \quad (4)$$

The intrinsic scatter of Γ is 0.32. CI are the blue contours in Fig. 3.

Note that removing the NLSy1s from our sample still gives a probability of having a positive correlation of 87%. If we do not consider objects with warm absorber, we have a probability of 85% to have a positive correlation.

The possible faint correlation between the photon index of the primary power-law and the soft-excess strength is also found in the case of reflection mainly due to a local reflector, with a Spearman correlation coefficient of $r=0.14$ and a null-hypothesis probability of 21%. We find the relation:

$$\Gamma = 0.11^{+0.08}_{-0.03} \times q + 1.71^{+0.001}_{-0.06} \quad (5)$$

The intrinsic scatter of Γ is 0.30.

If we only consider the 10 NLSy1 objects of our sample, Spearman statistics give a correlation coefficient of $r=0.50$, a

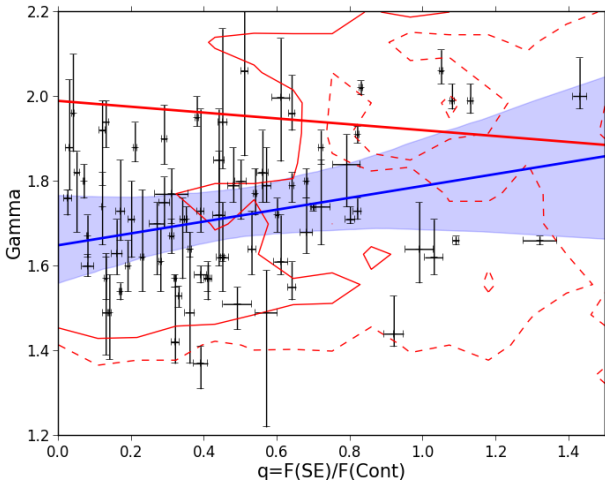


Fig. 3. Strength of the soft-excess against the power-law slope obtained with *XMM-Newton* and *BAT* data (in the case of distant reflection). CI are represented by the blue contours. The red line represents the relation expected in the case of ionized reflection; the red contours are the result of `relxillp_ion` simulations (solid line: 68%, dashed line: 90%).

null-hypothesis probability of 14% and a probability of 96% to have a positive correlation.

This correlation between the photon index and the soft-excess strength is consistent with the result of Page et al. (2004b), who found a correlation with a $\sim 4\%$ null-hypothesis probability obtained with seven objects observed by *XMM-Newton*.

The red line in Fig. 3 represents the relation between Γ and q expected in the case of ionized reflection. Density contours of the `relxillp_ion` simulations described in Sect. 4.2 are plotted in red (solid line: 68%, dashed line: 90%). Spearman statistics give a correlation coefficient of $r=-0.07$ and a null-hypothesis probability of $2 \times 10^{-5}\%$. The relation is:

$$\Gamma = -0.07^{+0.01}_{-0.01} \times q + 1.99^{+0.008}_{-0.008} \quad (6)$$

The results of the simulations are inconsistent with our observational results.

5.2. Reflection and photon index

We plot in Fig. 4 the reflection factor as a function of the photon index (in the case of reflection mainly due to a distant reflector). Spearman statistics show that a positive correlation exists between R and Γ ($r=0.35$ with a null-hypothesis probability of 0.02%). Using the Bayesian approach described in the previous sections, we perform a linear regression taking into account errors in x and y axes and intrinsic scatter. It results in the relation

$$R = 1.07^{+0.76}_{-0.37} \times \Gamma - 1.11^{+0.62}_{-1.34} \quad (7)$$

The intrinsic scatter is 0.17. The CI corresponding to this linear regression is represented by the blue contours in Fig. 4. This correlation between reflection and photon index has already been observed in previous works (Zdziarski et al. 1999; Lubiński & Zdziarski 2001; Perola et al. 2002; Mattson et al. 2007).

When removing the NLSy1s from our sample, the positive correlation between R and Γ remains with a Spearman correlation coefficient of $r=0.45$ and a null-hypothesis probability of

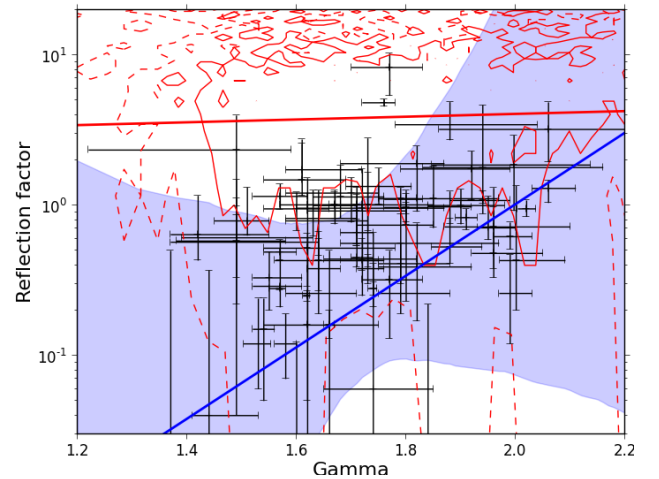


Fig. 4. Reflection factor against the power-law slope obtained with *XMM-Newton* and *BAT* data (in the case of distant reflection). CI are represented by the blue contours. The red line represent the relation between R and Γ in the case of ionized reflection. Density contours are plotted in red (solid line: 68%, dashed line: 90%).

0.006%. Considering objects with soft-excess without warm absorber, the probability of having a positive correlation is 99.2%.

In the case of a local-dominated reflection, we also find a steeper relation between Γ and R . Spearman statistics give a correlation factor of $r=0.33$ with a null-hypothesis probability of 0.2%. The correlation is characterized by the equation:

$$R = 1.27^{+0.23}_{-0.57} \times \Gamma - 0.93^{+0.55}_{-0.27} \quad (8)$$

The intrinsic scatter is 0.09.

Considering only NLSy1s, we obtain a Spearman correlation coefficient of $r=-0.11$, a null-hypothesis probability of 76% and a probability of 61% to have a negative correlation. However, the very flat slope of -0.007 obtained by linear regression is compatible, in view of its large uncertainties, with the positive relation found with the entire sample. The relation between R and Γ when we only consider NLSy1s is not statistically significant.

The red line and contours in Fig. 4 are the results expected in the case of ionized reflection. We can see that, according to `relxillp_ion` simulations described in Sect. 4.2, a weak correlation is expected between R and Γ (Spearman correlation coefficient $r=0.10$ with a null-hypothesis probability of $1 \times 10^{-8}\%$). The relation is:

$$R = 0.39^{+0.27}_{-0.27} \times \Gamma + 5.03^{+0.54}_{-0.55} \quad (9)$$

The slope found between R and Γ in the case of blurred ionized reflection is different with the one found in the data.

6. Spectra stacking

As we want to study the shape of the spectra for different soft-excess strengths, in both soft and hard X-ray energy bands, we stack *XMM-Newton EPIC/PN* and *Swift/BAT* spectra for four groups divided on the basis of their soft-excess strengths, considering values of q obtained when fitting the individual spectra in the case of distant-dominated reflection. The choice for the q ranges is made in order to have an equivalent number of spectra in each group (see Tab 1).

Before stacking the spectra, we renormalize each *PN* and *BAT* spectra to the same flux, to avoid any preponderance of spectral shape from objects with higher fluxes. We then stack *XMM-Newton/PN* and *Swift/BAT* spectra per groups of soft-excess strengths, using the `addspec` tool from `FTOOLS`² (Blackburn 1995). Top panel of Fig. 5 shows the resulting stacked *PN* and *BAT* spectra. The figure shows the evidence of different soft-excess strengths in the soft X-ray emission as expected, but no difference in the reflection strengths at higher energy. We measure the photon index and the reflection factor for each of the stacked spectra by fitting them between 3 and 100 keV with a `pexmon` model. The resulting parameters are presented in Tab 1. We see a clear increase of the value of the photon index per increasing soft-excess strength (as the possible correlation shown in Sect. 5.1), but we do not see any trend for the reflection factor, showing that the reflection strength and the soft-excess strength are not linked. The photon indexes vary when fitting together the *XMM-Newton/PN* and *Swift/BAT* stacked spectra of the four groups of different soft-excess strengths, although *BAT* spectra all look the same, because *XMM-Newton/PN* spectra have a more important weight in the fit than *BAT* spectra (because of their better signal-to-noise ratios). The value of Γ then strongly depends on the shape of *XMM-Newton* spectra, which look different between 3 and 10 keV for the different soft-excess

strengths. When fitting *BAT* stacked spectra alone, we cannot see any trend for Γ and R as a function of q , as photon indexes are similar for the four groups and reflection factors failed to be constrained. The absence of evolution of R in the stacked spectra, which is in contradiction with the anti-correlation found in our sample between R and q (see Sect. 4.1), may be due to low statistics.

The bottom panel of Fig. 5 shows the ratios of stacked spectra, calculated with `mathpha` (Blackburn 1995). We can see, in both panels, that the difference in spectral shape in the soft X-ray band is obvious for different soft-excess strengths. However, we do not notice any spectral shape difference in the hard X-ray band.

If we consider only the NLSy1s present in our sample and stack their *XMM-Newton* and *Swift/BAT* spectra for four groups of soft-excess strength, we observe the same trend as the one found for the entire sample. We see in Tab 1 that the photon

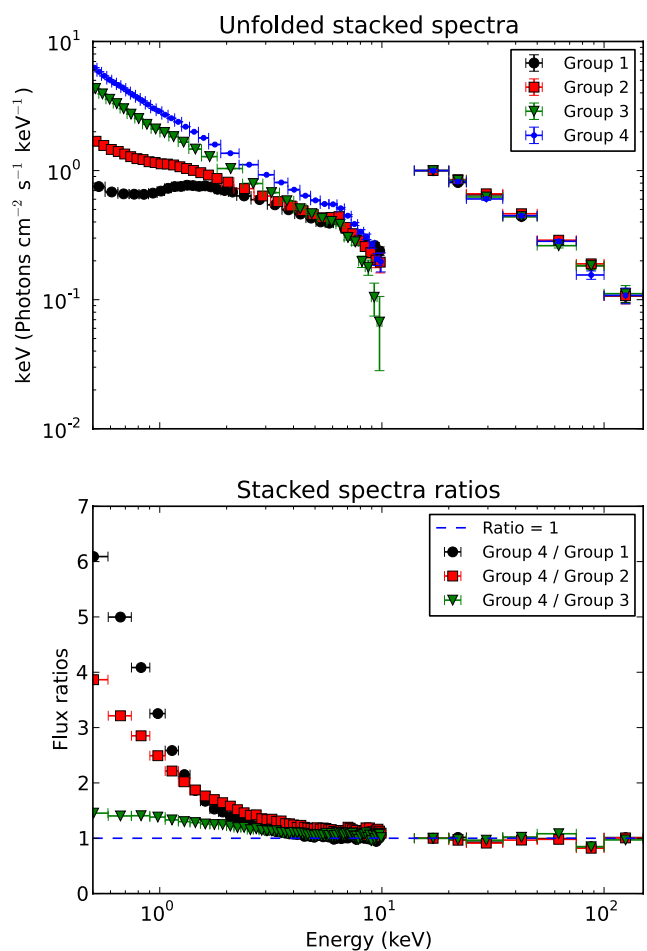


Fig. 5. Results of stacking spectra per soft-excess strengths. Top panel: Stacked *XMM-Newton/PN* and *Swift/BAT* spectra for the four groups of different q (normalized to the spectrum with smaller q value, at 15 keV). The q value is increasing for stacked spectra from black circles (Group 1) to red squares (Group 2), to green triangles (Group 3) and to blue dots (Group 4). Bottom panel: Ratios of the stacked *XMM-Newton/PN* and *Swift/BAT* spectra. The ratio of stacked spectra of higher q (Group 4) over lower q (Group 1) is represented in black circles; The ratio of stacked spectra from Group 3 over Group 1 is plotted in red squares; The ratio of Group 2 over Group 1 is in green triangles.

² <http://heasarc.gsfc.nasa.gov/ftools/>

Table 1. Results of the fitting on the stacked spectra using, on one hand, all the objects of our sample with a soft-excess, and on the other hand, NLSy1s only.

Group	Soft-excess strength	Total sample			NLSy1s		
		Objects	R	Γ	Objects	R	Γ
1	$q < 0.25$	19	0.69 ± 0.16	1.75 ± 0.05	2	0.53 ± 0.27	1.79 ± 0.06
2	$0.25 \leq q < 0.4$	19	0.97 ± 0.23	1.81 ± 0.06	3	1.01 ± 0.71	1.98 ± 0.08
3	$0.4 \leq q < 0.6$	20	0.60 ± 0.29	1.99 ± 0.08	2	0.59 ± 0.28	2.15 ± 0.08
4	$q \geq 0.6$	21	0.84 ± 0.16	2.04 ± 0.04	3	0.47 ± 0.10	2.29 ± 0.03

index is increasing for an increasing value of the soft-excess strength, but we do not note any evolution trend for the reflection factor.

7. Relation with the Eddington ratio

For 20 objects of our sample, Eddington ratios have been calculated by Ricci et al. (2013). They used average bolometric corrections k_x (taken from the literature) obtained from studies of the AGN spectral energy distribution to calculate the Eddington ratios. Considering black-hole masses from previous works of Woo & Urry (2002) and Vasudevan et al. (2010), we can easily calculate the Eddington ratios for 13 additional objects non studied in Ricci et al. (2013). The Eddington ratio is calculated as:

$$\lambda_{Edd} = \frac{L_{Bol}}{L_{Edd}} = \frac{k_x \times L_{2-10keV}}{1.26 \times 10^{38} \times M_{BH}/M_{\odot}} \quad (10)$$

We plot in Fig. 6 the photon index as a function of the Eddington ratio for the 33 NLSy1, Sy1 and Sy1.5 objects. A linear regression with `linmix_err` gives the following relation:

$$\Gamma = 0.13^{+0.05}_{-0.04} \times \log(\lambda_{Edd}) + 1.89^{+0.08}_{-0.03} \quad (11)$$

with a correlation coefficient of 0.47 and a null-hypothesis probability of 0.4%. The intrinsic scatter of Γ is 0.02. Such a positive correlation has already been found in several works performed using *ASCA*, *ROSAT*, *Swift* and *XMM-Newton* (Wang et al. 2004; Grupe 2004; Porquet et al. 2004; Bian et al. 2005; Grupe et al. 2010), establishing a relation between Γ and λ_{Edd} (Shemmer et al. 2008; Risaliti et al. 2009; Jin et al. 2012).

We plot in Fig. 7 the soft-excess strength as a function of the Eddington ratio. We find:

$$q = 0.28^{+0.01}_{-0.15} \times \log(\lambda_{Edd}) + 0.72^{+0.11}_{-0.09} \quad (12)$$

A correlation exists with a coefficient of 0.43 and is significant (null-hypothesis probability of 1%). The intrinsic scatter of q is 0.07.

We plot in Fig. 8 the reflection factor as a function of the Eddington ratio. The linear regression process leads to the relation:

$$\log(R) = 0.06^{+0.09}_{-0.08} \times \log(\lambda_{Edd}) - 0.09^{+0.10}_{-0.12} \quad (13)$$

The correlation between R and λ_{Edd} is not significant, as the correlation coefficient of 0.17 is obtained with a null-hypothesis probability of 31%. The intrinsic scatter of $\log(R)$ is 0.05.

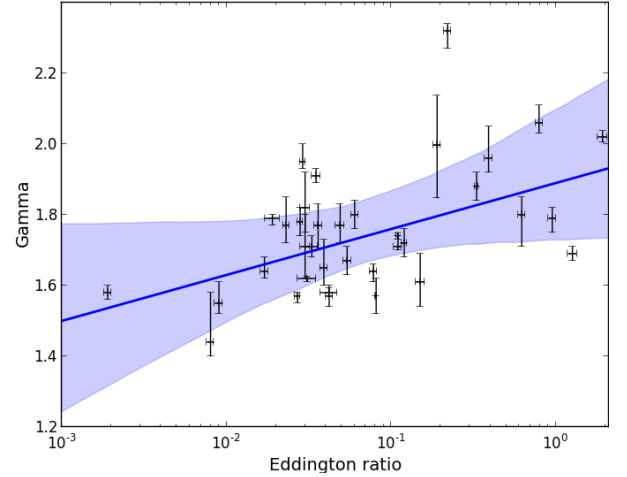


Fig. 6. Photon index of the primary continuum as a function of the Eddington ratio. Linear regression is represented by the blue line and 99% CI is given by the blue contour.

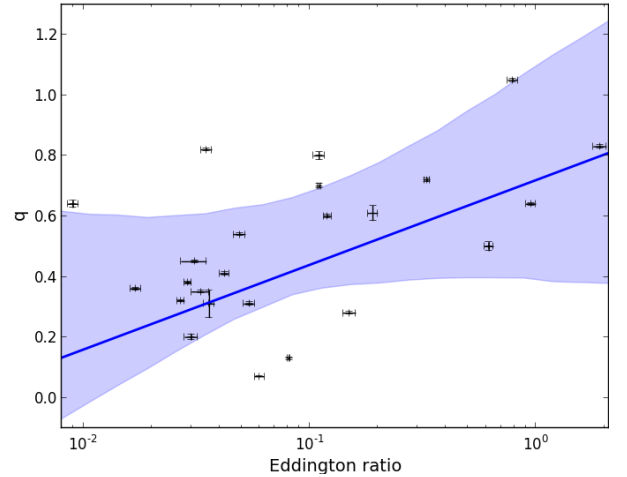


Fig. 7. Soft-excess strength as a function of the Eddington ratio. Linear regression is represented by the blue line and 99% CI is given by the blue contour.

8. Discussion

We studied 102 Seyfert 1s (Sy1.0, 1.2, 1.5, NLSy1) from the *Swift/BAT* 70-Months Hard X-ray Survey catalog, using *Swift/BAT* and *XMM-Newton* observations. The simultaneous spectral analysis of the soft and the hard X-ray emission aims

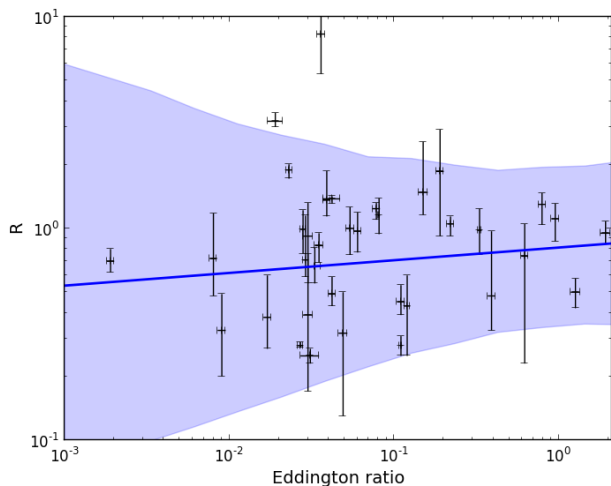


Fig. 8. Reflection factor as a function of the Eddington ratio. Linear regression is represented by the blue line and 99% CI is given by the blue contour.

to study the behavior between the soft-excess present in a large fraction of Seyfert 1s and the reflection component. We have seen that our results are not affected by the presence of NLSy1s in our sample, as the trends are similar or compatible when excluding these objects from our analysis or when considering only NLSy1s (relations found between q , R and Γ and stacking of spectra). This suggests that the mechanism responsible for the soft-excess is similar for all the categories of our sample. We did not find any effect of ionized absorption present in many objects of our sample. Our method to measure the soft-excess strength is robust even in objects with moderate absorption.

8.1. Link between soft-excess and reflection

Vasudevan et al. (2013) studied a sample of AGNs from the 58-month *Swift*/*BAT* catalog. Using *BAT* and *XMM-Newton* data, they constrained the reflection and the soft-excess strength in 39 sources. A plot of the reflection strength R against the soft-excess strength for the 23 low-absorption sources from Vasudevan et al. (2013) is presented in Figure 1 of Vasudevan et al. (2014). The figure shows strong hints of a correlation. This correlation can be explained by the fact that, in the case of local reflection, higher reflection leads to stronger emission lines below 1 keV that are smeared in the vicinity of the supermassive black hole, inducing a larger smooth bump at low energy, the soft-excess.

It is necessary to use simultaneous broad-band data in order to distinguish between mechanisms at the origin of the soft-excess. In Vasudevan et al. (2014), *XMM-Newton* and *NuSTAR* simulations are done to produce a plot of the strength of the hard X-ray emission (measured by a neutral reflection model) versus the strength of the soft-excess (modeled by a blackbody). This figure can be used as a diagnostic plot to determine the soft-excess production mechanism. Indeed, there is no evidence of a correlation between R and the soft-excess strength in the case of ionized absorption for example. But a correlation exists in the case of ionized reflection.

In our work, we use a larger sample than Vasudevan et al. (2014) (our sample contains ~ 3.5 times more sources) to produce a plot of the reflection factor versus the soft-excess strength, but we do not obtain the same results as the similar plot

of Vasudevan et al. (2014). Our work has 10 objects in common with their analysis (Vasudevan et al. 2013). For 4 of them (NGC 4593, NGC 5548, IC 2637 and Mrk 50), R and q values match both studies. For 4 other sources (Mrk 817, KUG 1141+371, QSO B1419+480 and NGC 4235), very small R and/or q values from the study of Vasudevan et al. (2014) have intermediate R and q values in our work. For NGC 4051, we obtain a smaller reflection factor than Vasudevan et al. (2014) and non-negligible absorption prevents the detection of a soft-excess. Mrk 766 gives us a similar value of the soft-excess strength, but a smaller value of R , compared to results from Vasudevan et al. (2014). We note that, in general, reflection factors measured in our work are rarely higher than 2, as spectral fitting results from Crummy et al. (2006) and Walton et al. (2013) who obtained in average $R \sim 1$, while Vasudevan et al. (2013) get higher R values. The correlation found in Vasudevan et al. (2014) seems to be driven by objects that show extreme values of R and q but whose measurements are unreliable. These differences between the results can be due to the fact that Vasudevan et al. (2013) used a different fitting process. Indeed, they fitted spectra from 1.5 keV with a *pexrav* model, ignoring the iron energy band (between 5.5 and 7.5 keV), fixing abundances, adding an absorber to the model and using a blackbody to model the soft-excess from 0.4 keV. They also used a different definition of q ($L_{BB,0.4-3\text{ keV}}/L_{\text{pow},1.5-6\text{ keV}}$). The cross-calibration method also differs. Indeed, Vasudevan et al. (2013) renormalized some *BAT* spectra, for objects whose soft X-ray observations have been taken within the timeframe of the *BAT* survey, using the *BAT* light curve and considering the ratio between *BAT* flux during the entire survey and *BAT* flux during the *XMM-Newton* observation. However, variability in AGN can happen also on time-scales shorter than a month, so this ratio might not be indicative of the real difference in flux between the short *XMM-Newton* observations and the 70-months averaged *Swift*/*BAT* flux.

After analyzing spectrally our sample of objects, we do not see any hint of correlation as found in the plot of the reflection versus the soft-excess strength of Vasudevan et al. (2014). We even find evidence of a weak anti-correlation between R and q (see blue contours in top panel of Fig. 2). We used the *relxillpion* model to simulate spectra, as we measure q and R differently compared to the work of Vasudevan et al. (2014). Our simulations are in good agreement with those carried out by Vasudevan et al. (2014). Indeed, as reported by Vasudevan et al. (2014), if the soft-excess was entirely due to blurred reflection, one would expect to find a correlation between the reflection factor and the soft-excess strength (see red line in top panel of Fig. 2). In this case, we should obtain high R and high q as well as small R and small q ($R < 2.0$ and $q < 0.75$, blue box in bottom panel of Fig. 2). The fact that most of the objects of our sample (75%) appear in the blue box is difficult to explain in the blurred ionized reflection hypothesis, as this model predicts that only 25% of the objects should appear as small- q , small- R . There is no easy way to restrict the parameter space to match the blue box. In particular, high- R , high- q objects are objects with intermediate ionization. Considering our sample of 79 Seyfert 1s, no positive correlation is found between R and q (both in the local and in the distant reflection scenario) and only small R and q values are measured (see bottom panel of Fig. 2). These contradictions are a strong argument against the ionized-reflection hypothesis as the origin of the soft-excess in most objects.

By stacking *XMM-Newton*/*PN* and *Swift*/*BAT* spectra in different bins of soft-excess intensity (see Fig. 5), we have seen that there is no obvious difference in the spectral shape in the hard X-ray band, in the individual stacked spectra and in their

ratios. While the spectra are steeper for a stronger soft-excess, we do not see any evolution of the reflection factor. We observe the same results when stacking NLSy1 spectra only. The values of the photon index we obtain are consistent with that found by Ricci et al. (2011) by stacking *INTEGRAL* spectra of type 1 and 1.5 AGN. There is no stronger reflection feature in the hard X-ray band for stronger soft-excess, as we would expect in the case where ionized reflection is at the origin of the soft-excess. This result suggests that the blurred ionized-reflection is not responsible for the existence of the soft-excess in most objects of our sample.

8.2. Soft-excess and X-ray continuum

Studying our 79 objects with soft-excess, we have found a possible correlation between the photon index of the primary continuum and the strength q of the soft-excess (see blue contours in Fig. 3). This trend is also verified when we consider the objects grouped per soft-excess strength, by fitting spectra stacked per soft-excess strengths (see Tab 1). Such a correlation has already been cautiously presented in Page et al. (2004b) with a higher significance than in this work. A possible faint anti-correlation between Γ and q is expected in the case of ionized reflection, as shown by `relxilllp_ion` simulations (see red line and contours in Fig. 3), which is at odds with the possible positive correlation found with our data. A positive correlation as the one found in our sample might suggest a connection between the soft-excess and the cooling of the hot corona. As proposed in the case of Mrk 509 (Petrucci et al. 2013), a warm corona could upscatter the optical-UV photons from the accretion disk to produce the soft-excess. This soft-excess could constitute a non-negligible part of the soft photons Comptonized in the hot corona (producing the primary X-ray continuum), as they would participate in its cooling. Indeed, the warm plasma emission peaks from a few eV to a few hundreds of eV, so it could be considered by the hot corona as a soft photon field with an intermediate temperature (see Figure 10 in Petrucci et al. 2013). The geometry of a hot photon-starved corona surrounded by an outer cold disk has already been suggested by Abramowicz et al. (1995) and Narayan & Yi (1995) and applied for example in NGC 4151 by Lubiński et al. (2010). Petrucci et al. (2013) propose that the plasma responsible for the soft-excess in Mrk 509 could be a warm upper layer of this accretion disk. In this case, a higher soft-excess strength q means a more efficient cooling and a softer X-ray emission. The relation between Γ and q is an argument in favour of warm Comptonization models to explain the soft-excess.

Studying the relation between R and Γ , we found a correlation with our 79 objects (see blue contours in Fig. 4). A faint correlation is also expected with ionized reflection (see red contours in Fig. 4), but the relation slopes are different. The mean value of $R \sim 5$ for the ionized reflection is due to the chosen parameters for the simulations. Indeed, we chose a reflection factor going up to 100 for the `relxilllp_ion` model, so the reflection factor R measured with `pexmon` is high. But this mean value of $R \sim 5$ resulting from simulations does not have a real meaning as the values of the other parameters are not known. Correlations have been found previously between the reflection and the power-law photon index in several works. Using *Ginga* spectra of radio-quiet Seyfert 1s and narrow emission-line galaxies, Zdziarski et al. (1999) found a very strong correlation between the intrinsic spectral slope in X-rays and the amount of Compton reflection from a cold medium ($R \propto \Gamma^{12}$). They interpreted this as being due to a feedback within the source where

the cold medium responsible for the reflection emits soft photons that irradiate the X-ray source and participate in the cooling as seeds for Compton upscattering. Fainter correlations have been also found between R and Γ and between the spectral slope and the strength of the iron line (Lubiński & Zdziarski 2001; Perola et al. 2002). Mattson et al. (2007) found a relation between R and Γ ($R = 0.54\Gamma - 0.87$), close to the one we found during our analysis ($R = 1.07^{+0.76}_{-0.37} \times \Gamma - 1.11^{+0.62}_{-1.34}$), that could be due to degeneracies during modeling process. According to Malzac & Petrucci (2002), the correlation between R and Γ could be due to the presence of a remote cold material. Indeed, assuming that disk reflection is negligible and hence that reflection is mainly due to distant cold material, fluctuations of primary X-ray emission slope at constant flux make the spectrum pivot, inducing a correlation between Γ and R . The correlation between R and Γ that we find for both local and distant reflection scenarii, as it differs from blurred ionized-reflection model expectations in slope, is an other argument against the ionized-reflection hypothesis as the origin of the soft-excess.

8.3. Relations with the Eddington ratio λ_{Edd}

A positive correlation has already been found between the photon index of the primary continuum and the Eddington ratio in several works (Wang et al. 2004; Grupe 2004; Porquet et al. 2004; Bian et al. 2005; Kelly 2007; Shemmer et al. 2008; Risaliti et al. 2009; Grupe et al. 2010; Jin et al. 2012). Shemmer et al. (2008) found the relation $\Gamma = 0.31 \log(\lambda_{Edd}) + 2.11$, consistent with results from Wang et al. (2004) and Kelly (2007). Risaliti et al. (2009) and Jin et al. (2012) found a steeper relation: $\Gamma \propto 0.60 \log(\lambda_{Edd})$. This relation implies a link between the accretion disk and the hot corona that could be due to the fact that the more accretion disk emits optical/UV photons, the more efficient the cooling of the corona. With our sample of 79 Seyfert 1s, we possibly found such a correlation between Γ and λ_{Edd} (see Fig. 6), with a flatter relation which is inconsistent with previous results ($\Gamma = 0.13 \log(\lambda_{Edd}) + 1.89$). The difference between our result and previous ones may be due to the different fitting procedures, as Shemmer et al. (2008), Risaliti et al. (2009) and Jin et al. (2012) used a simple absorbed power-law to fit their data.

As shown in Fig. 7, we found a possible correlation between λ_{Edd} and q . This might show a link between the accretion disk and the warm corona responsible for the soft-excess in the warm Comptonization model. In the case of Mrk 509, Petrucci et al. (2013) propose a geometry where the warm corona is the top layer of the accretion disk. The warm corona heats the deeper layers and Comptonizes their optical/UV photons, creating the soft-excess feature (see Figure 10 in Petrucci et al. 2013). Such a geometry could then explain the correlation between λ_{Edd} and q , which is an argument in favour of the warm Comptonization hypothesis as the origin of the soft-excess. As we find correlations between λ_{Edd} and q and between Γ and λ_{Edd} , a correlation between Γ and q , as the one found in Sect. 5.1, is expected, driven by λ_{Edd} .

The Baldwin effect, which is an anti-correlation between the equivalent width (EW) of the iron $K\alpha$ line and the X-ray luminosity ($EW \propto L_X^{-0.20}$ – Iwasawa & Taniguchi 1993), could be explained by the decrease of luminosity when the covering factor of the torus from the unification model increases (Page et al. 2004a; Bianchi et al. 2007). A similar trend has been observed between the EW of the Fe $K\alpha$ line and the Eddington ratio. Studying a large sample of unabsorbed AGN, Bianchi et al. (2007) found the relation $EW \propto \lambda_{Edd}^{-0.19}$, while Shu et al. (2010), using a sample of *Chandra/HEG* observations, found a similar

relation of $EW \propto (L_{2-10\text{keV}}/L_{Edd})^{-0.20}$ when fitting each observation, but a weaker correlation ($EW \propto (L_{2-10\text{keV}}/L_{Edd})^{-0.11}$) when doing the fits per source. Using results of Shu et al. (2010) and bolometric corrections, Ricci et al. (2013) found the relation $\log(EW) = -0.13 \log(\lambda_{Edd}) + 1.47$.

We found, in our work, an anti-correlation between R and q . We also found a positive correlation between q and λ_{Edd} . We then expect to have an anti-correlation between R and λ_{Edd} , similarly to the Baldwin effect, as the EW of the Fe $K\alpha$ line and the reflection factor R are both representative of the reflection strength. Unfortunately, probably due to intrinsic scatter and large uncertainties, this expected anti-correlation between R and λ_{Edd} is not seen in our sample.

A possible explanation for this anti-correlation between R and q is the warm Comptonization. In this scenario, a warm plasma, that could be the upper layer of the disk, upscatters the soft optical/UV photons from the disk to reproduce the soft-excess. The warm plasma being at a temperature of ~ 1 keV is highly ionized; reflection on this medium is largely featureless and follows the primary emission. Therefore, a disk covered with a warm plasma sees its reflection factor R decrease compared to the case with no or little warm plasma. Hence, the stronger the soft-excess, the smaller the reflection factor. The anti-correlation found in data between R and q could then be explained if the soft-excess comes from a warm plasma.

9. Conclusion

The nature of the soft-excess in AGN is still uncertain, as physical mechanisms used to model this feature are difficult to distinguish when analysing soft X-rays spectra. The *Swift*/*BAT* and *XMM-Newton* spectral analysis of a large sample of Seyfert 1s from the *Swift*/*BAT* 70-Months Hard X-ray Survey catalog allows a hard X-ray view of the soft-excess in AGN. We have fitted the 3-100 keV data with phenomenological model and then quantify the soft-excess below 2 keV with respect to this model. We found that 80% of the objects of our sample show the presence of a soft-excess.

We have shown, fitting the spectra of 79 Seyfert 1s lowly absorbed and showing a soft-excess, that the soft-excess strength and the reflection factor are not positively correlated. By stacking *XMM-Newton*/*PN* and *Swift*/*BAT* spectra per soft-excess strengths, we have shown that the reflection characterized by the Compton hump at about 30 keV does not vary with the soft-excess strength. These results are in contradiction with the correlation expected from ionized reflection, shown by our simulations with `relxillp_ion` and by simulations of *XMM-Newton* and *NuSTAR* spectra from Vasudevan et al. (2014). This contradiction between expectations and measurements is a strong argument against the ionized-reflection hypothesis as the origin of the soft-excess in most objects. The possible anti-correlation we found could be explained by a warm Comptonization scenario, where a warm plasma covering the disk would make the reflection featureless.

We have also seen that the strength of the soft-excess q is correlated with the spectral index Γ and with the Eddington ratio λ_{Edd} . This could be explained by warm Comptonization scenarios, such as the one described in Petrucci et al. (2013), where a higher q value might mean a more efficient cooling of the hot corona responsible for the primary X-ray emission and hence a steeper spectrum. Furthermore, the relation found between R and Γ is different from that found in `relxillp_ion` simulations and can be used as an additional argument against ionized reflection. The correlation could be due to the fact that the medium

responsible for reflection emits soft photons that participate in the cooling of the hot corona.

The relation found between R , Γ and q are found under the hypothesis of a reflection component mainly due to distant material, as well as if this reflection mainly comes from the accretion disk, which we cannot distinguish here.

This work suggests that the soft-excess present in 80% of the objects of our sample is, in most cases, likely not due to blurred ionized reflection, but can most probably be explained by warm Comptonization. Future works with *NuSTAR* and *ASTRO-H* will shed light on this issue, as the better signal-to-noise data they will provide in the hard X-ray band may allow to spectrally discriminate both models.

Table .2. List of the sources used for this study, with their spectral types, redshifts z , Galactic column densities (N_{H}^{G} values from Dickey & Lockman (1990)), and soft X-ray observations information (observation date, observation identification and net exposure).

Source	Type	z	N_{H}^{G} [10^{20} cm^{-2}]	Obs. date YYYY-MM-DD	Obs. ID	Net exposure [ks]
1H 0419–577	Sy 1.5	0.104	1.83	2010–05–30	0604720301	100.3
1H 2251–179 ^P	Sy 1.5	0.064	2.7	2002–05–18	0012940101	61.8
1RXS J213944.3+595016	Sy 1.5	0.114	59.7	2008–05–11	0555321001	8.7
2MASSi J1031543–141651	Sy 1.0	0.086	6.45	2004–12–19	0203770101	34.6
2MASX J18560128+1538059	Sy 1.0	0.084	37.4	2009–04–06	0550451601	6.2
2MASX J22484165–5109338	Sy 1.5	0.100	1.35	2007–05–15	0510380101	64.5
3C 111.0	Sy 1.0	0.048	32.2	2009–02–15	0552180101	71.8
3C 382	Sy 1.0	0.058	7.46	2008–04–28	0506120101	32.4
3C 390.3	Sy 1.5	0.056	4.28	2004–10–08	0203720201	51.7
4C +74.26	Sy 1.0	0.104	12.2	2004–02–06	0200910201	31.9
4U 0517+17	Sy 1.5	0.018	22.0	2007–08–21	0502090501	57.2
6dF J2132022–334254 ^P	Sy 1.2	0.030	4.07	2004–10–30	0201130301	46.0
Ark 120	Sy 1.0	0.032	12.6	2003–08–25	0147190101	105.3
CGCG 229–015	Sy 1.0	0.028	6.25	2011–06–05	0672530301	23.9
ESO 140–43	Sy 1.5	0.014	7.3	2005–09–08	0300240401	21.8
ESO 141–55 ^P	Sy 1.2	0.037	5.1	2007–10–30	0503750101	77.6
ESO 198–024	Sy 1.0	0.046	3.05	2006–02–04	0305370101	121.9
ESO 209–12	Sy 1.5	0.040	23.8	2006–03–25	0401790301	7.2
ESO 323–77	Sy 1.2	0.015	7.4	2006–02–07	0300240501	25.6
ESO 359– G 019	Sy 1.0	0.055	1.02	2004–03–09	0201130101	24.0
ESO 548–G081 ^P	Sy 1.0	0.014	3.04	2006–01–28	0312190601	10.0
EXO 055620–3820.2	Sy 1.2	0.034	4.0	2006–11–03	0404260301	75.9
Fairall 1116	Sy 1.0	0.058	3.09	2005–08–28	0301450301	20.1
Fairall 1146	Sy 1.0	0.032	40.3	2006–12–12	0401790401	11.6
Fairall 9	Sy 1.2	0.047	3.28	2009–12–09	0605800401	129.6
GQ Com	Sy 1.2	0.165	1.67	2002–05–30	0109080101	13.3
GRS 1734–292 ^P	Sy 1.0	0.021	76.7	2009–02–26	0550451501	12.1
[HB89] 0052+251	Sy 1.2	0.154	4.93	2005–06–26	0301450401	19.8
[HB89] 0119–286	Sy 1.0	0.116	1.65	2003–01–07	0110950201	5.7
[HB89] 0241+622	Sy 1.2	0.044	74.2	2008–02–28	0503690101	30.0
IC 0486	Sy 1.0	0.027	3.95	2007–10–28	0504101201	20.1
IC 2637	Sy 1.5	0.029	2.66	2009–12–20	0601780201	13.2
IC 4329A	Sy 1.2	0.016	4.4	2003–08–06	0147440101	118.4
IGR J00335+6126	Sy 1.5	0.105	61.6	2010–01–15	0601740101	21.5
IGR J07597–3842	Sy 1.2	0.040	60.3	2006–04–08	0303230101	15.0
IGR J11457–1827	Sy 1.5	0.033	3.5	2004–06–08	0201130201	31.0
IGR J12172+0710	Sy 1.2	0.008	1.5	2004–06–09	0204650201	9.3
IGR J13038+5348 ^P	Sy 1.2	0.029	1.6	2006–06–23	0312192001	9.6
IGR J13109–5552	Sy 1.0	0.104	27.6	2009–02–26	0550450901	17.9
IGR J16119–6036	Sy 1.5	0.016	23.1	2009–02–18	0550451101	13.1
IGR J16185–5928	NLSy 1	0.035	24.7	2009–02–18	0550451201	17.4
IGR J16482–3036	Sy 1.0	0.031	17.6	2006–03–01	0305831001	7.5
IGR J16558–5203	Sy 1.2	0.054	30.4	2006–03–01	0306171201	8.9
IGR J17418–1212	Sy 1.2	0.037	20.9	2006–04–04	0303230501	13.1
IGR J17488–3253	Sy 1.0	0.020	53.0	2007–03–03	0405390101	6.57
IGR J18027–1455	Sy 1.0	0.035	49.7	2006–03–25	0303230601	18.1
IGR J18259–0706	Sy 1.0	0.037	71.2	2011–03–07	0650591501	25.9
IGR J19378–0617	Sy 1.5	0.011	14.8	2009–04–28	0550451701	17.4
IGR J21277+5656	NLSy 1	0.015	78.7	2010–11–29	0655450101	127.5
IRAS 04392–2713	Sy 1.5	0.084	2.49	2005–08–13	0301450101	20.0
IRAS 15091–2107	NLSy 1	0.044	8.42	2005–07–26	0300240201	18.7
KUG 1141+371	Sy 1.0	0.038	1.90	2009–05–23	0601780501	5.4
LEDA 168563	Sy 1.0	0.029	54.2	2007–02–26	0401790201	10.5
MCG –02–14–009	Sy 1.0	0.028	9.23	2009–02–27	0550640101	79.1
MCG–02–58–022	Sy 1.5	0.047	3.60	2000–12–01	0109130701	10.3
MCG–06–30–015	Sy 1.5	0.008	4.08	2001–08–04	0029740801	124.0

Table .2. Information on sources and observations used. – *continued*

Source	Type	z	N_{H}^{G} [10^{20} cm^{-2}]	Obs. date YYYY-MM-DD	Obs. ID	Net exposure [ks]
MCG+08–11–011	Sy 1.5	0.020	20.9	2004–04–09	0201930201	30.4
Mrk 1040	Sy 1.0	0.016	7.22	2009–02–13	0554990101	66.8
Mrk 1044	NLSy 1	0.016	3.36	2013–01–27	0695290101	107.2
Mrk 110	NLSy 1	0.035	1.47	2004–11–15	0201130501	47
Mrk 1152	Sy 1.5	0.052	1.68	2003–06–15	0147920101	21.5
Mrk 279	Sy 1.0	0.030	1.78	2005–11–17	0302480501	49.2
Mrk 290	Sy 1.5	0.030	1.70	2006–05–06	0400360801	18.6
Mrk 335	NLSy 1	0.026	4.03	2006–01–03	0306870101	117.0
Mrk 352 ^P	Sy 1.0	0.015	5.59	2006–01–24	0312190101	10.8
Mrk 359	NLSy 1	0.017	4.79	2010–07–25	0655590201	24.8
Mrk 50	Sy 1.2	0.024	1.77	2010–12–09	0650590401	15.7
Mrk 509	Sy 1.5	0.034	4.11	2006–04–25	0306090401	61.8
Mrk 590	Sy 1.0	0.027	2.68	2004–07–04	0201020201	32.4
Mrk 6	Sy 1.5	0.019	6.39	2001–03–27	0061540101	26.0
Mrk 684 ^P	NLSy 1	0.046	1.46	2006–01–24	0300910101	11.1
Mrk 704	Sy 1.2	0.029	3.43	2008–11–02	0502091601	87.0
Mrk 739E	NLSy 1	0.029	1.90	2009–06–14	0601780401	10.0
Mrk 766	NLSy 1	0.013	1.71	2001–05–20	0109141301	121.4
Mrk 771	Sy 1.0	0.063	2.24	2005–07–09	0301450201	24.3
Mrk 79	Sy 1.2	0.022	5.73	2008–04–26	0502091001	67.6
Mrk 817 ^P	Sy 1.5	0.031	1.49	2009–12–13	0601781401	5.6
NGC 3227	Sy 1.5	0.004	2.15	2006–12–03	0400270101	101.3
NGC 3516	Sy 1.5	0.009	3.05	2001–11–09	0107460701	119.5
NGC 3783	Sy 1.5	0.010	8.50	2001–12–19	0112210501	127.5
NGC 4051	NLSy 1	0.002	1.32	2002–11–22	0157560101	48.2
NGC 4151	Sy 1.5	0.003	1.98	2000–12–22	0112830201	57.0
NGC 4593	Sy 1.0	0.009	2.31	2000–07–02	0109970101	10.1
NGC 5548	Sy 1.5	0.017	1.69	2001–07–09	0089960301	70.2
NGC 6814	Sy 1.5	0.005	12.8	2009–04–22	0550451801	28.4
NGC 7469	Sy 1.5	0.016	4.87	2004–11–30	0207090101	84.5
NGC 7603	Sy 1.5	0.030	4.09	2006–06–14	0305600601	16.4
NGC 985	Sy 1.5	0.043	2.9	2003–07–15	0150470601	57.6
PG 0804+761	Sy 1.0	0.100	2.98	2010–03–10	0605110101	42.8
PG 1501+106	Sy 1.5	0.036	2.34	2005–01–16	0205340201	46
PKS 0558–504	NLSy 1	0.137	4.50	2008–09–11	0555170401	123.3
PKS 2135–14	Sy 1.5	0.200	4.70	2001–04–28	0092850201	27.2
QSO B1419+480	Sy 1.5	0.072	1.65	2002–05–27	0094740201	20.1
QSO B1821+643	Sy 1.2	0.297	4.04	2007–12–10	0506210101	13.6
RHS 39	Sy 1.0	0.022	4.88	2007–08–05	0502090201	108.9
RX J2135.9+4728	Sy 1.0	0.025	38.6	2010–11–11	0650591701	22.8
SWIFT J0519.5–3140	Sy 1.0	0.013	1.76	2010–01–29	0610180101	76.5
SWIFT J0640.4–2554	Sy 1.0	0.026	11.4	2006–03–07	0312190801	10.3
SWIFT J0917.2–6221	Sy 1.0	0.057	19.1	2008–12–14	0550452601	16
SWIFT J1038.8–4942	Sy 1.0	0.060	27.2	2011–01–11	0650591101	24.9
SWIFT J2009.0–6103	Sy 1.5	0.015	4.2	2009–03–30	0552170301	92.9
UGC 3142	Sy 1.0	0.022	19.0	2007–03–18	0401790101	9.8

^P source presented pile-up and the extraction region used is an annulus of inner radius 15 arcsec

Table 3. EPIC-PN and MOS XMM-Newton and Swift/BAT data analysis.

Source	Γ	$F_{\text{continuum}} (2-10)$ $10^{-11} \text{ erg cm}^{-2} \text{ s}^{-1}$	$F_{\text{soft-excess}} (0.5-2)$ $10^{-11} \text{ erg cm}^{-2} \text{ s}^{-1}$	Model	q	R	χ^2/dof
1H 0419–577	1.79 ^{+0.03} _{-0.04}	1.08 ^{+0.002} _{-0.002}	0.43 ^{+0.003} _{-0.003}	2brem	0.64 ^{+0.005} _{-0.005}	1.11 ^{+0.20} _{-0.24}	4347/3996
1H2251–179	1.57 ^{+0.05} _{-0.05}	1.87 ^{+0.004} _{-0.004}	0.11 ^{+0.003} _{-0.003}	1brem + WA	0.13 ^{+0.004} _{-0.004}	1.15 ^{+0.24} _{-0.21}	3378/3199
1RXSJ213944.3+595016	1.69 ^{+0.09} _{-0.05}	0.55 ^{+0.005} _{-0.005}	–	Absorbed	–	0.27 ^{+0.46} _{-0.14}	654/643
2MASSi J1031543–141651	1.73 ^{+0.03} _{-0.02}	1.58 ^{+0.004} _{-0.004}	0.79 ^{+0.01} _{-0.01}	2brem	0.82 ^{+0.011} _{-0.011}	0.38 ^{+0.09} _{-0.08}	3039/3044
2MASX J18560128+1538059	1.73 ^{+0.12} _{-0.07}	1.03 ^{+0.005} _{-0.005}	0.10 ^{+0.007} _{-0.007}	Cold abs + 1brem	0.17 ^{+0.012} _{-0.012}	1.01 ^{+0.64} _{-0.33}	1489/1540
2MASX J22484165–5109338	1.64 ^{+0.09} _{-0.06}	0.38 ^{+0.009} _{+0.0009}	0.10 ^{+0.002} _{-0.002}	2brem	0.53 ^{+0.011} _{-0.011}	0.79 ^{+0.47} _{-0.33}	2202/2195
3C 111.0	1.54 ^{+0.02} _{-0.02}	3.92 ^{+0.005} _{-0.005}	0.29 ^{+0.006} _{-0.006}	Cold abs + 1brem	0.17 ^{+0.004} _{-0.004}	0.15 ^{+0.09} _{-0.10}	3430/3147
3C 382	1.77 ^{+0.06} _{-0.05}	3.48 ^{+0.006} _{-0.006}	1.14 ^{+0.01} _{-0.01}	2brem + WA	0.54 ^{+0.005} _{-0.005}	0.32 ^{+0.18} _{-0.19}	2794/2652
3C 390.3	1.57 ^{+0.01} _{-0.02}	3.43 ^{+0.007} _{-0.007}	0.52 ^{+0.006} _{-0.006}	2brem + WA	0.32 ^{+0.004} _{-0.004}	0.28 ^{+0.01} _{-0.007}	4863/4349
4C +74.26	1.78 ^{+0.04} _{-0.04}	1.83 ^{+0.003} _{-0.003}	–	Absorbed	–	0.99 ^{+0.23} _{-0.23}	4069/3680
4U 0517+17	1.67 ^{+0.05} _{-0.05}	2.31 ^{+0.004} _{-0.004}	0.10 ^{+0.002} _{-0.002}	1brem + WA	0.08 ^{+0.002} _{-0.002}	1.01 ^{+0.21} _{-0.19}	4789/4062
6dF J2132022–334254	1.42 ^{+0.13} _{-0.05}	0.79 ^{+0.004} _{-0.004}	0.09 ^{+0.003} _{-0.003}	2brem	0.32 ^{+0.011} _{-0.011}	0.64 ^{+0.52} _{-0.21}	2167/2193
Ark 120	1.91 ^{+0.02} _{-0.02}	2.97 ^{+0.003} _{-0.003}	1.83 ^{+0.008} _{-0.008}	2brem	0.82 ^{+0.004} _{-0.004}	0.83 ^{+0.12} _{-0.14}	5219/4654
CGCG 229–015	1.72 ^{+0.15} _{-0.12}	0.32 ^{+0.001} _{-0.001}	0.08 ^{+0.003} _{-0.003}	2brem	0.44 ^{+0.017} _{-0.017}	0.96 ^{+0.79} _{-0.59}	1520/1567
ESO 140–43	1.97 ^{+0.04} _{-0.05}	1.80 ^{+0.004} _{-0.004}	–	2brem + WA	–	2.15 ^{+0.28} _{-0.40}	2906/2570
ESO 141–55	1.95 ^{+0.05} _{-0.02}	2.82 ^{+0.006} _{-0.006}	0.85 ^{+0.01} _{-0.01}	2brem	0.38 ^{+0.005} _{-0.005}	0.71 ^{+0.44} _{-0.12}	3230/2789
ESO 198–024	1.64 ^{+0.04} _{-0.02}	0.81 ^{+0.001} _{-0.001}	0.15 ^{+0.002} _{-0.002}	2brem	0.36 ^{+0.005} _{-0.005}	0.38 ^{+0.22} _{-0.11}	2875/2780
ESO 209–12	1.68 ^{+0.08} _{-0.05}	0.68 ^{+0.005} _{-0.005}	0.25 ^{+0.006} _{-0.006}	1brem + WA	0.68 ^{+0.017} _{-0.017}	1.14 ^{+0.70} _{-0.32}	1075/1034
ESO 323–77	–	–	–	Clumpy torus + BLR ^(a)	–	–	–
ESO 359–G 019	1.51 ^{+0.04} _{-0.06}	0.25 ^{+0.002} _{-0.002}	0.05 ^{+0.004} _{-0.004}	2brem	0.49 ^{+0.039} _{-0.039}	0.79 ^{+0.53} _{-0.16}	1013/1012
ESO 548–G081	1.55 ^{+0.06} _{-0.03}	1.18 ^{+0.008} _{-0.008}	0.50 ^{+0.009} _{-0.009}	1brem + WA	0.64 ^{+0.012} _{-0.012}	0.33 ^{+0.16} _{-0.13}	1055/1024
EXO 055620–3820.2	–	–	–	Ionized absorber ^(b)	–	–	–
Fairall 1116	1.79 ^{+0.09} _{-0.04}	0.60 ^{+0.003} _{-0.003}	0.18 ^{+0.006} _{-0.006}	2brem	0.48 ^{+0.016} _{-0.016}	0.41 ^{+0.54} _{-0.11}	1593/1559
Fairall 1146	2.07 ^{+0.07} _{-0.08}	0.80 ^{+0.006} _{-0.006}	–	1brem + WA	–	3.08 ^{+0.62} _{-0.71}	1633/1583
Fairall 9	1.71 ^{+0.03} _{-0.03}	1.64 ^{+0.002} _{-0.002}	0.32 ^{+0.004} _{-0.004}	2brem	0.35 ^{+0.004} _{-0.004}	0.66 ^{+0.15} _{-0.11}	3396/2997
GQ Com	1.62 ^{+0.13} _{-0.08}	0.41 ^{+0.004} _{-0.004}	0.09 ^{+0.003} _{-0.003}	2brem	0.45 ^{+0.016} _{-0.016}	0.16 ^{+0.49} _{-0.16}	649/604
GRS 1734–292	1.70 ^{+0.04} _{-0.02}	5.28 ^{+0.02} _{-0.02}	–	Absorbed	–	0.19 ^{+0.14} _{-0.10}	2033/1971
[HB89] 0052+251	1.62 ^{+0.09} _{-0.04}	0.57 ^{+0.003} _{-0.003}	0.29 ^{+0.007} _{-0.007}	2brem	1.03 ^{+0.025} _{-0.025}	0.26 ^{+0.35} _{-0.21}	1580/1635
[HB89] 0119–286	1.84 ^{+0.07} _{-0.10}	0.41 ^{+0.007} _{-0.007}	0.22 ^{+0.01} _{-0.01}	2brem	0.79 ^{+0.038} _{-0.038}	2 × 10 ⁻⁶ ^{+0.22} _{-2 × 10⁻⁶}	404/410
[HB89] 0241+622	1.60 ^{+0.06} _{-0.06}	1.89 ^{+0.004} _{-0.004}	0.17 ^{+0.004} _{-0.004}	Cold abs + 1brem	0.19 ^{+0.005} _{-0.005}	0.95 ^{+0.27} _{-0.27}	3635/3507

Table 3. EPIC-PN and MOS XMM-Newton and Swift/BAT data analysis. – continued

Source	Γ	$F_{\text{continuum}} (2-10)$ $10^{-11} \text{ erg cm}^{-2} \text{ s}^{-1}$	$F_{\text{soft-excess}} (0.5-2)$ $10^{-11} \text{ erg cm}^{-2} \text{ s}^{-1}$	Model	q	R	χ^2/dof
IC 0486	1.57 ^{+0.16} _{-0.11}	0.43 ^{+0.004} _{-0.004}	–	2WA	–	1.47 ^{+1.16} _{-0.22}	840/709
IC 2637	1.62 ^{+0.16} _{-0.08}	0.36 ^{+0.003} _{-0.003}	0.04 ^{+0.0009} _{-0.0009}	1brem	0.23 ^{+0.005} _{-0.005}	0.52 ^{+1.00} _{-0.23}	861/889
IC 4329A	1.69 ^{+0.02} _{-0.02}	8.17 ^{+0.006} _{-0.006}	–	3WA + Abs + 1brem ^(c)	–	0.50 ^{+0.08} _{-0.08}	7521/5093
IGR J00335+6126	1.88 ^{+0.15} _{-0.11}	0.29 ^{+0.003} _{-0.003}	–	Cold abs + 1brem	–	5.94 ^{+3.39} _{-1.64}	898/778
IGR J07597–3842	1.63 ^{+0.08} _{-0.05}	1.38 ^{+0.006} _{-0.006}	0.11 ^{+0.01} _{-0.01}	1brem + WA	0.16 ^{+0.02} _{-0.02}	0.82 ^{+0.44} _{-0.20}	2102/2130
IGR J11457–1827	1.66 ^{+0.01} _{-0.01}	2.30 ^{+0.005} _{-0.005}	1.31 ^{+0.01} _{-0.01}	2brem	1.09 ^{+0.009} _{-0.009}	0.16 ^{+0.04} _{-0.03}	2736/2533
IGR J12172+0710	1.49 ^{+0.09} _{-0.11}	0.53 ^{+0.006} _{-0.006}	0.03 ^{+0.001} _{-0.001}	Cold abs + 1brem	0.14 ^{+0.005} _{-0.005}	0.58 ^{+0.28} _{-0.25}	538/550
IGR J13038+5348	1.58 ^{+0.02} _{-0.02}	1.21 ^{+0.006} _{-0.006}	0.21 ^{+0.009} _{-0.009}	2brem	0.39 ^{+0.02} _{-0.02}	0.12 ^{+0.07} _{-0.05}	1790/1764
IGR J13109–5552	1.37 ^{+0.04} _{-0.06}	0.47 ^{+0.003} _{-0.003}	0.06 ^{+0.003} _{-0.003}	1brem	0.39 ^{+0.02} _{-0.02}	4 × 10 ⁻⁹ _{-4 × 10⁻⁹}	1167/1159
IGR J16119–6036	1.70 ^{+0.05} _{-0.12}	0.60 ^{+0.004} _{-0.004}	0.09 ^{+0.007} _{-0.007}	2brem	0.27 ^{+0.02} _{-0.02}	1.21 ^{+0.32} _{-0.44}	1232/1196
IGR J16185–5928	1.49 ^{+0.10} _{-0.27}	0.17 ^{+0.003} _{-0.003}	0.04 ^{+0.002} _{-0.002}	1brem	0.57 ^{+0.03} _{-0.03}	2.34 ^{+1.63} _{-1.35}	410/412
IGR J16482–3036	1.53 ^{+0.02} _{-0.03}	1.61 ^{+0.007} _{-0.007}	0.22 ^{+0.005} _{-0.005}	Cold abs + 1brem	0.33 ^{+0.008} _{-0.008}	0.12 ^{+0.12} _{-0.06}	2037/1780
IGR J16558–5203	1.64 ^{+0.11} _{-0.08}	1.06 ^{+0.007} _{-0.007}	0.51 ^{+0.02} _{-0.02}	2brem	0.99 ^{+0.04} _{-0.04}	0.43 ^{+0.24} _{-0.24}	1514/1490
IGR J17418–1212	1.88 ^{+0.06} _{-0.03}	1.48 ^{+0.007} _{-0.007}	0.22 ^{+0.005} _{-0.005}	Cold abs + 1brem	0.21 ^{+0.005} _{-0.005}	0.53 ^{+0.29} _{-0.12}	2112/2047
IGR J17488–3253	1.60 ^{+0.03} _{-0.03}	1.29 ^{+0.009} _{-0.009}	0.05 ^{+0.01} _{-0.01}	Cold abs + 1brem	0.08 ^{+0.02} _{-0.02}	2 × 10 ⁻³ _{-2 × 10⁻³}	758/785
IGR J18027–1455	1.49 ^{+0.14} _{-0.10}	0.80 ^{+0.006} _{-0.006}	0.04 ^{+0.003} _{-0.003}	Cold abs + 1brem	0.13 ^{+0.009} _{-0.009}	0.61 ^{+0.51} _{-0.39}	1177/1215
IGR J18259–0706	1.75 ^{+0.06} _{-0.06}	0.70 ^{+0.003} _{-0.003}	0.12 ^{+0.006} _{-0.006}	Cold abs + 1brem	0.29 ^{+0.02} _{-0.02}	1.34 ^{+0.43} _{-0.32}	1926/1872
IGR J19378–0617	2.00 ^{+0.09} _{-0.03}	1.98 ^{+0.009} _{-0.009}	2.45 ^{+0.03} _{-0.03}	2brem + WA	1.43 ^{+0.02} _{-0.02}	0.43 ^{+0.92} _{-0.23}	1175/1139
IGR J21277+5656	2.04 ^{+0.04} _{-0.03}	1.81 ^{+0.002} _{-0.002}	–	WA	–	1.50 ^{+0.25} _{-0.16}	4992/4378
IRAS 04392–2713	2.06 ^{+0.16} _{-0.20}	0.49 ^{+0.002} _{-0.002}	0.16 ^{+0.003} _{-0.003}	2brem	0.51 ^{+0.01} _{-0.01}	3.21 ^{+1.65} _{-1.27}	1632/1586
IRAS 15091–2107	1.82 ^{+0.05} _{-0.14}	0.61 ^{+0.003} _{-0.003}	0.02 ^{+0.003} _{-0.003}	Cold abs + 1brem	0.05 ^{+0.007} _{-0.007}	1.90 ^{+0.59} _{-0.99}	1778/1668
KUG 1141+371	1.49 ^{+0.15} _{-0.12}	0.21 ^{+0.003} _{-0.003}	0.03 ^{+0.001} _{-0.001}	1brem	0.36 ^{+0.013} _{-0.013}	0.57 ^{+0.92} _{-0.53}	289/315
LEDA 168563	1.66 ^{+0.01} _{-0.01}	3.03 ^{+0.007} _{-0.007}	2.03 ^{+0.07} _{-0.07}	2brem	1.32 ^{+0.05} _{-0.05}	2 × 10 ⁻¹⁰ _{-2 × 10⁻¹⁰}	3114/2959
MCG –02–14–009	1.90 ^{+0.08} _{-0.06}	0.51 ^{+0.001} _{-0.001}	0.11 ^{+0.003} _{-0.003}	2brem	0.29 ^{+0.008} _{-0.008}	1.00 ^{+0.28} _{-0.25}	2073/1984
MCG –02–58–022	1.74 ^{+0.08} _{-0.09}	3.84 ^{+0.009} _{-0.009}	0.26 ^{+0.005} _{-0.005}	1brem	0.12 ^{+0.002} _{-0.002}	0.44 ^{+0.22} _{-0.23}	1780/1756
MCG –06–30–015	2.32 ^{+0.02} _{-0.05}	4.69 ^{+0.01} _{-0.01}	–	3WA + Abs ^(d)	–	1.05 ^{+0.09} _{-0.13}	9970/4823
MCG +08–11–011	1.67 ^{+0.04} _{-0.04}	3.48 ^{+0.006} _{-0.006}	0.56 ^{+0.01} _{-0.01}	2brem + WA	0.31 ^{+0.006} _{-0.006}	1.00 ^{+0.26} _{-0.25}	3139/2907
Mrk 1040	1.80 ^{+0.04} _{-0.04}	2.09 ^{+0.002} _{-0.002}	0.09 ^{+0.002} _{-0.002}	Abs + 2WA + 1brem ^(c)	0.07 ^{+0.002} _{-0.002}	0.97 ^{+0.22} _{-0.20}	4896/4336
Mrk 1044	1.99 ^{+0.04} _{-0.03}	0.92 ^{+0.001} _{-0.001}	0.90 ^{+0.006} _{-0.006}	2brem + WA	1.13 ^{+0.008} _{-0.008}	0.62 ^{+0.15} _{-0.11}	3773/3440
Mrk 110	1.80 ^{+0.05} _{-0.09}	2.43 ^{+0.006} _{-0.006}	0.68 ^{+0.02} _{-0.02}	2brem	0.50 ^{+0.02} _{-0.02}	0.74 ^{+0.31} _{-0.51}	2041/2010
Mrk 1152	1.71 ^{+0.05} _{-0.14}	0.32 ^{+0.002} _{-0.002}	0.06 ^{+0.001} _{-0.001}	1brem + WA	0.34 ^{+0.006} _{-0.006}	1.01 ^{+0.17} _{-0.47}	1178/1311

Table 3. *EPIC-PN* and *MOS XMM-Newton* and *Swift/BAT* data analysis. – continued

Source	Γ	$F_{\text{continuum}} (2-10)$ $10^{-11} \text{ erg cm}^{-2} \text{ s}^{-1}$	$F_{\text{soft-excess}} (0.5-2)$ $10^{-11} \text{ erg cm}^{-2} \text{ s}^{-1}$	Model	q	R	χ^2/dof
Mrk 279	1.74 ^{+0.007} _{-0.01}	1.69 ^{+0.004} _{-0.004}	0.64 ^{+0.006} _{-0.006}	2brem	0.70 ^{+0.007} _{-0.007}	0.28 ^{+0.03} _{-0.03}	1564/1557
Mrk 290	1.61 ^{+0.08} _{-0.07}	0.52 ^{+0.002} _{-0.002}	0.07 ^{+0.001} _{-0.001}	1brem + WA	0.28 ^{+0.004} _{-0.004}	1.48 ^{+1.09} _{-0.32}	1613/1569
Mrk 335	2.06 ^{+0.05} _{-0.03}	1.24 ^{+0.001} _{-0.001}	1.23 ^{+0.007} _{-0.007}	2brem + WA	1.05 ^{+0.006} _{-0.006}	1.30 ^{+0.17} _{-0.26}	4860/4275
Mrk 352	1.44 ^{+0.09} _{-0.03}	0.91 ^{+0.006} _{-0.006}	0.31 ^{+0.009} _{-0.009}	2brem	0.92 ^{+0.027} _{-0.027}	0.04 ^{+0.33} _{-0.04}	1498/1459
Mrk 359	1.85 ^{+0.12} _{-0.10}	0.60 ^{+0.003} _{-0.003}	0.18 ^{+0.006} _{-0.006}	2brem	0.44 ^{+0.02} _{-0.02}	1.11 ^{+0.72} _{-0.40}	1313/1307
Mrk 50	1.92 ^{+0.07} _{-0.13}	0.70 ^{+0.002} _{-0.002}	0.06 ^{+0.004} _{-0.004}	2brem	0.12 ^{+0.008} _{-0.008}	1.75 ^{+0.55} _{-0.67}	1993/1857
Mrk 509	1.72 ^{+0.04} _{-0.04}	3.58 ^{+0.004} _{-0.004}	1.22 ^{+0.01} _{-0.01}	2brem + WA	0.60 ^{+0.005} _{-0.005}	0.43 ^{+0.17} _{-0.18}	4846/4325
Mrk 590	1.57 ^{+0.03} _{-0.03}	0.49 ^{+0.001} _{-0.001}	0.09 ^{+0.001} _{-0.001}	1brem	0.41 ^{+0.005} _{-0.005}	0.49 ^{+0.10} _{-0.06}	2614/2513
Mrk 6	1.44 ^{+0.14} _{-0.04}	1.16 ^{+0.008} _{-0.008}	–	2WA + Abs + 1brem ^(f)	–	0.72 ^{+0.46} _{-0.24}	1095/1058
Mrk 684	1.74 ^{+0.11} _{-0.09}	0.36 ^{+0.003} _{-0.003}	0.15 ^{+0.005} _{-0.005}	2brem	0.72 ^{+0.03} _{-0.03}	0.06 ^{+0.35} _{-0.06}	803/848
Mrk 704	1.94 ^{+0.05} _{-0.06}	1.24 ^{+0.002} _{-0.002}	0.13 ^{+0.009} _{-0.009}	1brem + 2WA	0.13 ^{+0.009} _{-0.009}	1.08 ^{+0.17} _{-0.20}	4115/3649
Mrk 739E	1.96 ^{+0.14} _{-0.09}	0.67 ^{+0.003} _{-0.003}	0.02 ^{+0.002} _{-0.002}	Cold abs + 1brem	0.04 ^{+0.004} _{-0.004}	0.72 ^{+0.59} _{-0.34}	1121/1171
Mrk 766	2.02 ^{+0.02} _{-0.02}	1.70 ^{+0.002} _{-0.002}	1.25 ^{+0.008} _{-0.008}	2WA + 2brem	0.83 ^{+0.005} _{-0.005}	0.95 ^{+0.13} _{-0.11}	4276/2981
Mrk 771	1.79 ^{+0.09} _{-0.04}	0.42 ^{+0.003} _{-0.003}	0.15 ^{+0.003} _{-0.003}	2brem	0.57 ^{+0.01} _{-0.01}	0.26 ^{+0.30} _{-0.07}	1379/1338
Mrk 79	1.77 ^{+0.06} _{-0.07}	0.32 ^{+0.001} _{-0.001}	0.06 ^{+0.009} _{-0.009}	1brem + WA	0.31 ^{+0.05} _{-0.05}	8.29 ^{+1.98} _{-2.92}	2309/2226
Mrk 817	2.00 ^{+0.14} _{-0.15}	0.97 ^{+0.009} _{-0.009}	0.51 ^{+0.02} _{-0.02}	2brem	0.61 ^{+0.03} _{-0.03}	1.86 ^{+1.07} _{-0.94}	750/733
NGC 3227	1.58 ^{+0.02} _{-0.02}	2.97 ^{+0.003} _{-0.003}	–	3WA + 2brem ^(g)	–	0.70 ^{+0.10} _{-0.08}	5787/4816
NGC 3516	1.79 ^{+0.01} _{-0.02}	1.91 ^{+0.009} _{-0.009}	–	3WA ^(h)	–	3.21 ^{+0.31} _{-0.19}	8131/4424
NGC 3783	1.64 ^{+0.02} _{-0.03}	4.06 ^{+0.005} _{-0.005}	–	2WA + 2brem ⁽ⁱ⁾	–	1.24 ^{+0.08} _{-0.14}	2332/1896
NGC 4051	1.77 ^{+0.08} _{-0.05}	0.84 ^{+0.002} _{-0.002}	–	WA + 1brem ^(j)	–	1.89 ^{+0.12} _{-0.17}	7602/2576
NGC 4151	1.58 ^{+0.01} _{-0.002}	6.70 ^{+0.02} _{-0.02}	–	2WA + Abs ^(k)	–	1.38 ^{+0.04} _{-0.07}	19675/4849
NGC 4593	1.71 ^{+0.03} _{-0.01}	2.73 ^{+0.01} _{-0.01}	1.22 ^{+0.02} _{-0.02}	2brem + WA	0.80 ^{+0.01} _{-0.01}	0.45 ^{+0.09} _{-0.06}	1191/1195
NGC 5548	1.62 ^{+0.005} _{-0.009}	2.92 ^{+0.003} _{-0.003}	0.64 ^{+0.006} _{-0.006}	2brem + 2WA	0.45 ^{+0.004} _{-0.004}	0.25 ^{+0.02} _{-0.02}	3526/3230
NGC 6814	1.71 ^{+0.09} _{-0.09}	1.90 ^{+0.004} _{-0.004}	0.22 ^{+0.01} _{-0.01}	2brem	0.20 ^{+0.009} _{-0.009}	0.92 ^{+0.40} _{-0.37}	2641/2453
NGC 7469	1.88 ^{+0.04} _{-0.04}	2.42 ^{+0.003} _{-0.003}	1.26 ^{+0.01} _{-0.01}	2brem + WA	0.72 ^{+0.006} _{-0.006}	0.98 ^{+0.26} _{-0.23}	1701/1734
NGC 7603	1.82 ^{+0.10} _{-0.07}	2.11 ^{+0.01} _{-0.01}	0.78 ^{+0.02} _{-0.02}	2brem	0.56 ^{+0.02} _{-0.02}	0.39 ^{+0.37} _{-0.22}	1035/1007
NGC 985	1.65 ^{+0.08} _{-0.05}	0.82 ^{+0.004} _{-0.004}	–	1brem + WA	–	1.36 ^{+0.51} _{-0.22}	3034/2710
PG 0804+761	1.96 ^{+0.09} _{-0.04}	1.11 ^{+0.005} _{-0.005}	0.57 ^{+0.008} _{-0.008}	2brem	0.64 ^{+0.009} _{-0.009}	0.48 ^{+0.49} _{-0.15}	1841/1784
PG 1501+106	1.61 ^{+0.11} _{-0.03}	0.80 ^{+0.004} _{-0.004}	0.23 ^{+0.007} _{-0.007}	2brem + WA	0.61 ^{+0.02} _{-0.02}	1.73 ^{+1.02} _{-0.27}	2022/1998
PKS 0558–504	1.99 ^{+0.04} _{-0.02}	1.15 ^{+0.002} _{-0.002}	1.05 ^{+0.006} _{-0.006}	2brem	1.08 ^{+0.006} _{-0.006}	0.26 ^{+0.21} _{-0.14}	1864/1626
PKS 2135–14	1.57 ^{+0.04} _{-0.05}	0.43 ^{+0.002} _{-0.002}	0.08 ^{+0.002} _{-0.002}	2brem	0.41 ^{+0.01} _{-0.01}	0.29 ^{+0.20} _{-0.08}	1889/1964

Table 3. EPIC-PN and MOS XMM-Newton and Swift/BAT data analysis. – continued

Source	Γ	$F_{\text{continuum}} (2-10)$ $10^{-11} \text{ erg cm}^{-2} \text{ s}^{-1}$	$F_{\text{soft-excess}} (0.5-2)$ $10^{-11} \text{ erg cm}^{-2} \text{ s}^{-1}$	Model	q	R	χ^2/dof
QSO B1419+480	$1.73^{+0.24}_{-0.05}$	$0.52^{+0.004}_{-0.004}$	$0.14^{+0.003}_{-0.003}$	1brem + WA	$0.39^{+0.009}_{-0.009}$	$0.56^{2.24}_{-0.17}$	1333/1274
QSO B1821+643	$1.94^{+0.22}_{-0.11}$	$0.96^{+0.004}_{-0.004}$	$0.34^{+0.01}_{-0.01}$	2brem	$0.45^{+0.01}_{-0.01}$	$1.79^{2.87}_{-0.76}$	1830/1762
RHS 39	$1.80^{+0.03}_{-0.04}$	$1.37^{+0.002}_{-0.002}$	$0.59^{+0.004}_{-0.004}$	2brem	$0.68^{+0.005}_{-0.005}$	$1.10^{+0.16}_{-0.22}$	4788/4368
RX J2135.9+4728	$1.88^{+0.16}_{-0.10}$	$0.51^{+0.002}_{-0.002}$	$0.01^{+0.004}_{-0.004}$	1brem + WA	$0.03^{+0.01}_{-0.01}$	$3.45^{1.43}_{-0.73}$	1962/1893
SWIFT J0519.5–3140	$1.76^{+0.02}_{-0.04}$	$0.47^{+0.001}_{-0.001}$	$0.02^{+0.007}_{-0.007}$	1brem + WA	$0.03^{+0.01}_{-0.01}$	$4.83^{+0.26}_{-0.27}$	3845/3582
SWIFT J0640.4–2554	$1.61^{+0.03}_{-0.03}$	$1.94^{+0.009}_{-0.009}$	–	Absorbed	–	$0.27^{+0.50}_{-0.27}$	2261/2120
SWIFT J0917.2–6221	$1.88^{+0.06}_{-0.07}$	$1.25^{+0.01}_{-0.01}$	–	2WA + Abs + 2brem	–	$0.60^{+0.23}_{-0.15}$	1194/1039
SWIFT J1038.8–4942	$1.58^{+0.05}_{-0.17}$	$0.64^{+0.01}_{-0.01}$	–	2WA + Abs + 2brem	–	$0.99^{+0.54}_{-1.86}$	750/576
SWIFT J2009.0–6103	$1.77^{+0.04}_{-0.05}$	$1.56^{+0.004}_{-0.004}$	–	2WA	–	$0.98^{+0.18}_{-0.22}$	7232/4266
UGC 3142	$1.41^{+0.02}_{-0.03}$	$2.18^{+0.02}_{-0.02}$	–	2WA + Abs + 3brem ^(f)	–	$0.61^{+0.05}_{-0.06}$	1543/1223

Models: *brem*: Bremsstrahlung models; WA: warm absorption; *Abs/Cold abs*: cold absorption.

References: (a) Miniutti et al. (2014); (b) Turner et al. (1996); (c) Steenbrugge et al. (2005); (d) Miyakawa et al. (2012); (e) Reynolds et al. (1995); (f) Mingo et al. (2011); (g) Noda et al. (2014); (h) Huerta et al. (2014); (i) Brenneman et al. (2011); (j) Pounds & King (2013); (k) Wang et al. (2011); (l) Ricci et al. (2010).

Acknowledgements. We would like to thank the referee for her useful comments which helped to improve this paper. We also acknowledge D. Eckert for useful discussion and L. Gibaud for her help in reducing data. RB acknowledges a grant from the Swiss National Science Foundation. CR acknowledges financial support from the Japan Society for the Promotion of Science (JSPS), CONICYT-Chile "EMBIGGEN" Anillo (grant ACT1101), from FONDECYT 1141218 and Basal-CATA PFB-06/2007. This research has made use of the NASA/IPAC Extragalactic Database (NED) which is operated by the Jet Propulsion Laboratory, of data obtained from the High Energy Astrophysics Science Archive Research Center (HEASARC), provided by NASA's Goddard Space Flight Center and of the SIMBAD Astronomical Database which is operated by the Centre de Données astronomiques de Strasbourg. This work was based on observations obtained with *XMM-Newton*, an ESA science mission with instruments and contributions directly funded by ESA Member States and NASA.

References

- Abramowicz, M. A., Chen, X., Kato, S., Lasota, J.-P., & Regev, O. 1995, *ApJ*, 438, L37
- Antonucci, R. 1993, *ARA&A*, 31, 473
- Arnaud, K. A. 1996, in *Astronomical Society of the Pacific Conference Series*, Vol. 101, *Astronomical Data Analysis Software and Systems V*, ed. G. H. Jacoby & J. Barnes, 17
- Arnaud, K. A., Branduardi-Raymont, G., Culhane, J. L., et al. 1985, *MNRAS*, 217, 105
- Barthelmy, S. D., Barbier, L. M., Cummings, J. R., et al. 2005, *Space Sci. Rev.*, 120, 143
- Baumgartner, W. H., Tueller, J., Markwardt, C. B., et al. 2013, *ApJS*, 207, 19
- Beuchert, T., Markowitz, A., Dauser, T., et al. 2014, in *The X-ray Universe 2014*, 228
- Bian, W. H., Zhao, Y. H., & Cheng, L. P. 2005, in *IAU Colloq. 199: Probing Galaxies through Quasar Absorption Lines*, ed. P. Williams, C.-G. Shu, & B. Menard, 400–402
- Bianchi, S., Guainazzi, M., Matt, G., & Fonseca Bonilla, N. 2007, *A&A*, 467, L19
- Bianchi, S., Guainazzi, M., Matt, G., Fonseca Bonilla, N., & Ponti, G. 2009, *A&A*, 495, 421
- Bianchi, S., La Franca, F., Matt, G., et al. 2008, *MNRAS*, 389, L52
- Blackburn, J. K. 1995, in *Astronomical Society of the Pacific Conference Series*, Vol. 77, *Astronomical Data Analysis Software and Systems IV*, ed. R. A. Shaw, H. E. Payne, & J. J. E. Hayes, 367
- Blandford, R. D., Netzer, H., Woltjer, L., Courvoisier, T. J.-L., & Mayor, M., eds. 1990, *Active Galactic Nuclei*
- Boissay, R., Paltani, S., Ponti, G., et al. 2014, *A&A*, 567, A44
- Brenneman, L. W., Reynolds, C. S., Nowak, M. A., et al. 2011, *ApJ*, 736, 103
- Cackett, E. M., Fabian, A. C., Zoghbi, A., et al. 2013, *ApJ*, 764, L9
- Crummy, J., Fabian, A. C., Gallo, L., & Ross, R. R. 2006, *MNRAS*, 365, 1067
- Dauser, T., García, J., Parker, M. L., Fabian, A. C., & Wilms, J. 2014, *MNRAS*, 444, L100
- De Marco, B., Ponti, G., Cappi, M., et al. 2013, *MNRAS*, 431, 2441
- De Marco, B., Ponti, G., Uttley, P., et al. 2011, *MNRAS*, 417, L98
- Di Gesu, L., Costantini, E., Piconcelli, E., et al. 2014, *A&A*, 563, A95
- Dickey, J. M. & Lockman, F. J. 1990, *ARA&A*, 28, 215
- Done, C., Jin, C., Middleton, M., & Ward, M. 2013, *MNRAS*, 434, 1955
- Done, C. & Nayakshin, S. 2007, *MNRAS*, 377, L59
- Edelson, R. A., Alexander, T., Crenshaw, D. M., et al. 1996, *ApJ*, 470, 364
- Fabian, A. C., Miniutti, G., Gallo, L., et al. 2004, *MNRAS*, 353, 1071
- Fabian, A. C., Miniutti, G., Iwasawa, K., & Ross, R. R. 2005, *MNRAS*, 361, 795
- Fabian, A. C., Rees, M. J., Stella, L., & White, N. E. 1989, *MNRAS*, 238, 729
- Fabian, A. C., Zoghbi, A., Ross, R. R., et al. 2009, *Nature*, 459, 540
- Fabian, A. C., Zoghbi, A., Wilkins, D., et al. 2012, *MNRAS*, 419, 116
- Gabriel, C., Denby, M., Fyfe, D. J., et al. 2004, in *Astronomical Society of the Pacific Conference Series*, Vol. 314, *Astronomical Data Analysis Software and Systems (ADASS) XIII*, ed. F. Ochsnein, M. G. Allen, & D. Egret, 759
- Gandhi, P., Höning, S. F., & Kishimoto, M. 2015, *ApJ*, 812, 113
- García, J., Dauser, T., Lohfink, A., et al. 2014, *ApJ*, 782, 76
- Gardner, E. & Done, C. 2014, *MNRAS*, 442, 2456
- Gehrels, N., Chincarini, G., Giommi, P., et al. 2004, *ApJ*, 611, 1005
- George, I. M. & Fabian, A. C. 1991, *MNRAS*, 249, 352
- George, I. M., Turner, T. J., Netzer, H., et al. 1998, *ApJS*, 114, 73
- Gierliński, M. & Done, C. 2004, *MNRAS*, 349, L7
- Grupe, D. 2004, *AJ*, 127, 1799
- Grupe, D., Komossa, S., Leighly, K. M., & Page, K. L. 2010, *ApJS*, 187, 64
- Haba, Y., Terashima, Y., Kunieda, H., & Ohsuga, K. 2008, *Advances in Space Research*, 41, 174
- Halpern, J. P. 1984, *ApJ*, 281, 90
- Huerta, E. M., Krongold, Y., Nicastro, F., et al. 2014, *ApJ*, 793, 61
- Iwasawa, K. & Taniguchi, Y. 1993, *ApJ*, 413, L15
- Jaffe, W., Meisenheimer, K., Röttgering, H. J. A., et al. 2004, *Nature*, 429, 47
- Jansen, F., Lumb, D., Altieri, B., et al. 2001, *A&A*, 365, L1
- Jin, C., Done, C., Ward, M., Gierliński, M., & Mullaney, J. 2009, *MNRAS*, 398, L16
- Jin, C., Ward, M., & Done, C. 2012, *MNRAS*, 425, 907
- Kara, E., Fabian, A. C., Cackett, E. M., et al. 2013, *MNRAS*, 434, 1129
- Kelly, B. C. 2007, *ApJ*, 665, 1489
- Krolik, J. H. 1999, *Active Galactic Nuclei: From the Central Black Hole to the Galactic Environment* / Princeton U Press, 1999 (Princeton Univ. Press)
- Lohfink, A. M., Reynolds, C. S., Mushotzky, R. F., & Nowak, M. A. 2013, *Mem. Soc. Astron. Italiana*, 84, 699
- Lubiński, P. & Zdziarski, A. A. 2001, *MNRAS*, 323, L37
- Lubiński, P., Zdziarski, A. A., Walter, R., et al. 2010, *MNRAS*, 408, 1851
- Magdziarz, P., Blaes, O. M., Zdziarski, A. A., Johnson, W. N., & Smith, D. A. 1998, *MNRAS*, 301, 179
- Magdziarz, P. & Zdziarski, A. A. 1995, *MNRAS*, 273, 837
- Malzac, J. & Petrucci, P.-O. 2002, *MNRAS*, 336, 1209
- Marinucci, A., Matt, G., Kara, E., et al. 2014, *MNRAS*, 440, 2347
- Matt, G., Marinucci, A., Guainazzi, M., et al. 2014, *MNRAS*, 439, 3016
- Matt, G., Perola, G. C., & Piro, L. 1991, *A&A*, 247, 25
- Mattson, B. J., Weaver, K. A., & Reynolds, C. S. 2007, *ApJ*, 664, 101
- Mehdipour, M., Branduardi-Raymont, G., Kaastra, J. S., et al. 2011, *A&A*, 534, A39
- Meisenheimer, K., Tristram, K. R. W., Jaffe, W., et al. 2007, *A&A*, 471, 453
- Middleton, M., Done, C., Ward, M., Gierliński, M., & Schurch, N. 2009, *MNRAS*, 394, 250
- Mingo, B., Hardcastle, M. J., Croston, J. H., et al. 2011, *ApJ*, 731, 21
- Miniutti, G. & Fabian, A. C. 2004, *MNRAS*, 349, 1435
- Miniutti, G., Sanfrutos, M., Beuchert, T., et al. 2014, *MNRAS*, 437, 1776
- Miyakawa, T., Ebisawa, K., & Inoue, H. 2012, *PASJ*, 64, 140
- Nandra, K., O'Neill, P. M., George, I. M., & Reeves, J. N. 2007, *MNRAS*, 382, 194
- Narayan, R. & Yi, I. 1995, *ApJ*, 452, 710
- Noda, H., Makishima, K., Nakazawa, K., et al. 2013, *PASJ*, 65, 4
- Noda, H., Makishima, K., Yamada, S., et al. 2014, *ApJ*, 794, 2
- Noda, H., Makishima, K., Yamada, S., et al. 2011, *PASJ*, 63, 925
- Page, K. L., O'Brien, P. T., Reeves, J. N., & Turner, M. J. L. 2004a, *MNRAS*, 347, 316
- Page, K. L., Schartel, N., Turner, M. J. L., & O'Brien, P. T. 2004b, *MNRAS*, 352, 523
- Parker, M. L., Wilkins, D. R., Fabian, A. C., et al. 2014, *MNRAS*, 443, 1723
- Patrick, A. R., Reeves, J. N., Porquet, D., et al. 2011, *MNRAS*, 411, 2353
- Perola, G. C., Matt, G., Cappi, M., et al. 2002, *A&A*, 389, 802
- Petrucci, P.-O., Paltani, S., Malzac, J., et al. 2013, *A&A*, 549, A73
- Piconcelli, E., Jimenez-Bailón, E., Guainazzi, M., et al. 2005, *A&A*, 432, 15
- Ponti, G., Cappi, M., Costantini, E., et al. 2013, *A&A*, 549, A72
- Ponti, G., Miniutti, G., Cappi, M., et al. 2006, *MNRAS*, 368, 903
- Porquet, D., Reeves, J. N., O'Brien, P., & Brinkmann, W. 2004, *A&A*, 422, 85
- Pounds, K. A. & King, A. R. 2013, *MNRAS*, 433, 1369
- Pounds, K. A., Warwick, R. S., Culhane, J. L., & de Korte, P. A. J. 1986, *MNRAS*, 218, 685
- Raban, D., Jaffe, W., Röttgering, H., Meisenheimer, K., & Tristram, K. R. W. 2009, *MNRAS*, 394, 1325
- Reynolds, C. S., Fabian, A. C., & Inoue, H. 1995, *MNRAS*, 276, 1311
- Ricci, C., Beckmann, V., Audard, M., & Courvoisier, T. J.-L. 2010, *A&A*, 518, A47
- Ricci, C., Paltani, S., Ueda, Y., & Awaki, H. 2013, *MNRAS*, 435, 1840
- Ricci, C., Ueda, Y., Paltani, S., et al. 2014, *MNRAS*, 441, 3622
- Ricci, C., Walter, R., Courvoisier, T. J.-L., & Paltani, S. 2011, *A&A*, 532, A102
- Risaliti, G., Young, M., & Elvis, M. 2009, *ApJ*, 700, L6
- Ross, R. R. & Fabian, A. C. 2005, *MNRAS*, 358, 211
- Schurch, N. J. & Done, C. 2007, *MNRAS*, 381, 1413
- Schurch, N. J., Done, C., & Proga, D. 2009, *ApJ*, 694, 1
- Scott, A. E., Stewart, G. C., & Mateos, S. 2012, *MNRAS*, 423, 2633
- Shakura, N. I. & Sunyaev, R. A. 1973, *A&A*, 24, 337
- Shemmer, O., Brandt, W. N., Netzer, H., Maiolino, R., & Kaspi, S. 2008, *ApJ*, 682, 81
- Shu, X. W., Yaqoob, T., & Wang, J. X. 2010, *ApJS*, 187, 581
- Shu, X. W., Yaqoob, T., & Wang, J. X. 2011, *ApJ*, 738, 147
- Singh, K. P., Garmire, G. P., & Nousek, J. 1985, *ApJ*, 297, 633
- Steenbrugge, K. C., Kaastra, J. S., Sako, M., et al. 2005, *A&A*, 432, 453
- Strüder, L., Briel, U., Dennerl, K., et al. 2001, *A&A*, 365, L18
- Turner, M. J. L., Abbey, A., Arnaud, M., et al. 2001, *A&A*, 365, L27
- Turner, T. J., Netzer, H., & George, I. M. 1996, *ApJ*, 463, 134
- Turner, T. J. & Pounds, K. A. 1989, *MNRAS*, 240, 833
- Vasudevan, R. V., Brandt, W. N., Mushotzky, R. F., et al. 2013, *ApJ*, 763, 111

- Vasudevan, R. V., Fabian, A. C., Gandhi, P., Winter, L. M., & Mushotzky, R. F. 2010, *MNRAS*, 402, 1081
- Vasudevan, R. V., Mushotzky, R. F., Reynolds, C. S., et al. 2014, *ApJ*, 785, 30
- Vaughan, S. & Fabian, A. C. 2004, *MNRAS*, 348, 1415
- Vaughan, S., Reeves, J., Warwick, R., & Edelson, R. 1999, *MNRAS*, 309, 113
- Véron-Cetty, M.-P. & Véron, P. 2010, *A&A*, 518, A10
- Walter, R. & Fink, H. H. 1993, *A&A*, 274, 105
- Walton, D. J., Nardini, E., Fabian, A. C., Gallo, L. C., & Reis, R. C. 2013, *MNRAS*, 428, 2901
- Wang, J., Fabbiano, G., Elvis, M., et al. 2011, *ApJ*, 742, 23
- Wang, J.-M., Watarai, K.-Y., & Mineshige, S. 2004, *ApJ*, 607, L107
- Woo, J.-H. & Urry, C. M. 2002, *ApJ*, 579, 530
- Zdziarski, A. A., Johnson, W. N., Done, C., Smith, D., & McNaron-Brown, K. 1995, *ApJ*, 438, L63
- Zdziarski, A. A., Johnson, W. N., & Magdziarz, P. 1996, *MNRAS*, 283, 193
- Zdziarski, A. A., Lubiński, P., & Smith, D. A. 1999, *MNRAS*, 303, L11
- Zoghbi, A., Fabian, A. C., & Gallo, L. C. 2008, *MNRAS*, 391, 2003
- Zoghbi, A., Fabian, A. C., Reynolds, C. S., & Cackett, E. M. 2012, *MNRAS*, 422, 129
- Zoghbi, A., Reynolds, C., Cackett, E. M., et al. 2013, *ApJ*, 767, 121